



HAL
open science

Observed spatio-temporal variability of the eddy-sea ice interactions in the Arctic Basin

Angelina Cassianides, Camille Lique, Anne-Marie Treguier, Gianluca Meneghello, Charly de Marez

► **To cite this version:**

Angelina Cassianides, Camille Lique, Anne-Marie Treguier, Gianluca Meneghello, Charly de Marez. Observed spatio-temporal variability of the eddy-sea ice interactions in the Arctic Basin. *Journal of Geophysical Research. Oceans*, 2023, 128 (6), e2022JC019469 (22p.). 10.1029/2022JC019469 . hal-04204076

HAL Id: hal-04204076

<https://hal.science/hal-04204076>

Submitted on 14 Sep 2023

HAL is a multi-disciplinary open access archive for the deposit and dissemination of scientific research documents, whether they are published or not. The documents may come from teaching and research institutions in France or abroad, or from public or private research centers.

L'archive ouverte pluridisciplinaire **HAL**, est destinée au dépôt et à la diffusion de documents scientifiques de niveau recherche, publiés ou non, émanant des établissements d'enseignement et de recherche français ou étrangers, des laboratoires publics ou privés.



Distributed under a Creative Commons Attribution 4.0 International License

Observed Spatio-Temporal Variability of the Eddy-Sea Ice Interactions in the Arctic Basin



Key Points:

- We use large datasets of in situ observations to document the Arctic dynamics at meso and submeso scales over 16 years
- In the ice pack the distribution of oceanic energy across scales is not determined at first order by the heterogeneity in sea ice conditions
- Subsurface eddy can potentially imprint a signature in sea ice drift and vorticity

Correspondence to:

A. Cassianides,
angelina.cassianides@ifremer.fr

Citation:

Cassianides, A., Lique, C., Tréguier, A.-M., Meneghello, G., & De Marez, C. (2023). Observed spatio-temporal variability of the eddy-sea ice interactions in the Arctic Basin. *Journal of Geophysical Research: Oceans*, 128, e2022JC019469. <https://doi.org/10.1029/2022JC019469>

Received 8 NOV 2022
Accepted 31 MAY 2023

Angéline Cassianides¹ , Camille Lique¹ , Anne-Marie Tréguier¹ , Gianluca Meneghello² , and Charly De Marez³

¹Univ. Brest, CNRS, IRD, Ifremer, Laboratoire d'Océanographie Physique et Spatiale, IUEM, Brest, France, ²Department of Earth, Atmospheric and Planetary Sciences, Massachusetts Institute of Technology, Cambridge, MA, USA, ³California Institute of Technology, Pasadena, CA, USA

Abstract In the Arctic Basin, the ocean dynamics at mesoscale and submesoscale under sea ice are poorly quantified and understood. Here, we analyze comprehensive data sets from Ice Tethered Profilers and moorings from the Beaufort Gyre Observing System spanning the period 2004–2019 in order to characterize the space and time variations of the (sub)mesoscale flow. In seasonally ice-covered regions, the dynamics in the surface layer is largely determined by the presence of sea ice, with an increased eddy kinetic energy and numerous eddies in summer. Beyond these regions, the influence of the sea ice conditions on the first order dynamics is less clear. A wavenumber spectra analysis of observations at the surface and at depth under the sea ice pack reveals that a large variety of regimes can be found, independently of the time and space variations of the sea ice conditions. Focusing on a census of individual eddies, and their potential signature in sea ice, we found that around 500 eddies can be detected in the subsurface layer over 2004–2019, including both submesoscale (radius between 3 and 10 km) and mesoscale (up to 80 km) structures. Based on simple scaling calculations, we quantify the dynamical or thermodynamical signature that these eddies may imprint at the surface. While they do not induce any significant heat flux and subsequent sea ice melt, subsurface eddies can induce a dynamic height anomaly of the order of a few centimetres, resulting into a surface vorticity anomaly strong enough to impact sea ice locally.

Plain Language Summary The presence of sea ice in the Arctic is thought to play a role for the determination of the ocean circulation, in particular for the small scale energetic eddies. Here, we revisit 16 years of temperature, salinity and velocity observations from moorings and autonomous profilers drifting with sea ice to characterize the spatio-temporal variations of the turbulent flow. On the one hand, there is a clear separation between the ice covered and the ice free regions: at first order the presence of sea ice damps the turbulence and dissipates surface eddies. Yet, under the sea ice pack, we find a large variety of turbulent regimes, that does not appear to be directly determined by the sea ice conditions. On the other hand, eddies propagating at depth under sea ice can potentially impact the sea ice, by exerting a stress strong enough to modify the sea ice drift and vorticity locally.

1. Introduction

The Arctic region is characterized by its fast-changing sea ice conditions. Over the past decades, the Arctic sea ice has transitioned toward a state with a much reduced extent, thinner thickness and faster drift (Meier & Stroeve, 2022; Meredith et al., 2022). As a consequence, the Arctic sea ice is also becoming more vulnerable to extreme synoptic events in the atmosphere or the ocean. For instance, an episode of strong winds in the Beaufort Sea in winter 2013 was found to have driven an intense, large scale breakup event (Rheinländer et al., 2022). On the ocean side, there is a general recognition that the presence of eddies can modulate the sea ice conditions. In the Marginal Ice Zone (MIZ), the examination of images from aerial surveys (J. Johannessen et al., 1987) or satellites (Kozlov et al., 2019) clearly reveals that sea ice is carrying the signature of ocean turbulence (eddies, filaments...). Based on data gathered during the MIZEX campaigns in the 1980's, J. Johannessen et al. (1987) and O. M. Johannessen et al. (1987) were able to describe for the first time the observed properties of both some subsurface eddies and their signature in the sea ice conditions. Using recent observations in the same region, von Appen et al. (2018) show how the presence of a submesoscale filament extending down to 250 m depth can modify the sea ice drift and as such strongly modulate the shape of the MIZ. More recently, studies often based on idealized process models have resulted in a process-based understanding of these signatures. Manucharyan

© 2023. The Authors.

This is an open access article under the terms of the [Creative Commons Attribution License](https://creativecommons.org/licenses/by/4.0/), which permits use, distribution and reproduction in any medium, provided the original work is properly cited.

and Thompson (2017) revealed how sea ice tends to be trapped in cyclonic eddies via mechanical stirring, where enhanced vertical heat flux leads to intensified sea ice melt (Gupta et al., 2020). Horvat et al. (2016) and Gupta and Thompson (2022) further showed that ocean eddies are affecting the thermodynamic growth/melt of sea ice, modulating the floe size distribution as well. Based on simple scaling arguments applied to observations, Cassianides et al. (2021) suggested that, locally, eddy could be the primary driver of sea ice drift and vorticity. It remains, however, to determine the potential importance of these processes for the evolution of sea ice at the scale of the Arctic Basin.

One reason of our limited understanding of the eddy imprint on sea ice is arguably that our knowledge of the Arctic dynamics at small scales is itself limited. The Arctic Basin is characterized by a very small Rossby radius of deformation (R_d), around 10 km in the interior and 1–2 km on the shelves (Nurser & Bacon, 2014). Given our focus on the interior of the basin, we refer in the following to *mesoscale* for the range of scales R_d – $10R_d$ (10–100 km), and *submesoscale* for the range smaller than 10 km, adopting the nomenclature of Callies and Ferrari (2013) and Klein et al. (2008). We note however that R_d does exhibit both temporal and spatial variations (resulting largely from the variations in stratification) that we do not consider in our analysis. Given the difficulty to simulate the Arctic at such a small Rossby radius, there are only a handful of models able to provide us with a description of the Arctic dynamics at (sub)mesoscale. Two noticeable exceptions are the descriptions of the spatio-temporal variations in Eddy Kinetic Energy (EKE) from high resolution models recently proposed by Regan et al. (2020) and Wang et al. (2020), which are largely consistent with the estimates of EKE obtained locally from mooring observations (von Appen et al., 2022). Turning our attention to observational studies, the picture is a bit different. Small coherent eddies have been randomly sampled by in situ observations under sea ice since the 1970's (Manley & Hunkins, 1985; Newton et al., 1974), and, given their small length scales (a few kilometers), these features were referred to as Submesoscale Coherent Vortices (SCV, D'Asaro, 1988). The recent development of autonomous observing systems adapted to ice-covered regions such as Ice Tethered Profiler (ITP, Toole et al., 2011) has led to more extensive eddy censuses over the period 2005–2015 (Zhao et al., 2014, 2016). These censuses have revealed that the Arctic halocline is populated with numerous small eddies (diameters of 1–15 km), the vast majority of which are anticyclones. Observations of the most recent period (after 2015) have not been used yet for that purpose. In addition to the description of individual SCV, in situ observations have also been used to examine the horizontal variability in potential energy under sea ice, based on wavenumber spectra performed along individual transects (Marcinko et al., 2015; Timmermans et al., 2012), and it was suggested that the presence of sea ice could damp the level of potential and kinetic energy at submesoscale (Mensa & Timmermans, 2017; Timmermans et al., 2012).

Despite their patchiness, observations and results from eddy-resolving models have also revealed that the small scale dynamics differs largely between layers in the Arctic, likely because of the presence of sea ice. In the surface layer, eddies are generated by a large variety of processes such as mixed layer instabilities at surface fronts (e.g., Brannigan et al., 2017) or intense brine rejection in leads and polynyas (Horvat et al., 2016; Woodgate et al., 2000). However, if they remain in the surface layer, these eddies are quickly dissipated by sea ice-induced friction, especially in winter when sea ice is the thickest and sustains larger internal stress (Ou & Gordon, 1986). Moreover, sea ice-induced friction also tends to make the surface layer baroclinically stable, thus reducing the generation of eddies (Manley & Hunkins, 1985; Meneghello et al., 2021). Deeper in the water column, the picture is different. There, eddies formed through baroclinic instabilities (Meneghello et al., 2021) or shed from the coastal and boundary currents (e.g., Pickart & Stossmeister, 2008; Spall, 2013) likely propagate freely independently from the presence of sea ice (Ou & Gordon, 1986). It remains unknown, however, if these subsurface eddies could imprint any signature on sea ice through dynamical or thermodynamical processes.

Here, we aim at characterizing the (sub)mesoscale variability in the different layers of the Arctic Ocean, exploiting fully the 16-years long ITP data set completed with moorings from the Beaufort Gyre Observing System (BGOS). We seek observational-based evidences and a better understanding of the interplay between the Arctic dynamics at small scales and sea ice. The remainder of this paper is organized as follows. The various observational datasets used in our analysis are presented in Section 2. We then quantify the time and space variations of the energy at the (sub)mesoscale in the surface layer (Section 3) and in the subsurface layer (Section 4) and put them in regard with the variations in sea ice conditions. We then perform a census of the coherent structures, and examine their potential interactions with sea ice (Section 5). Discussions and conclusion are given in Section 6.

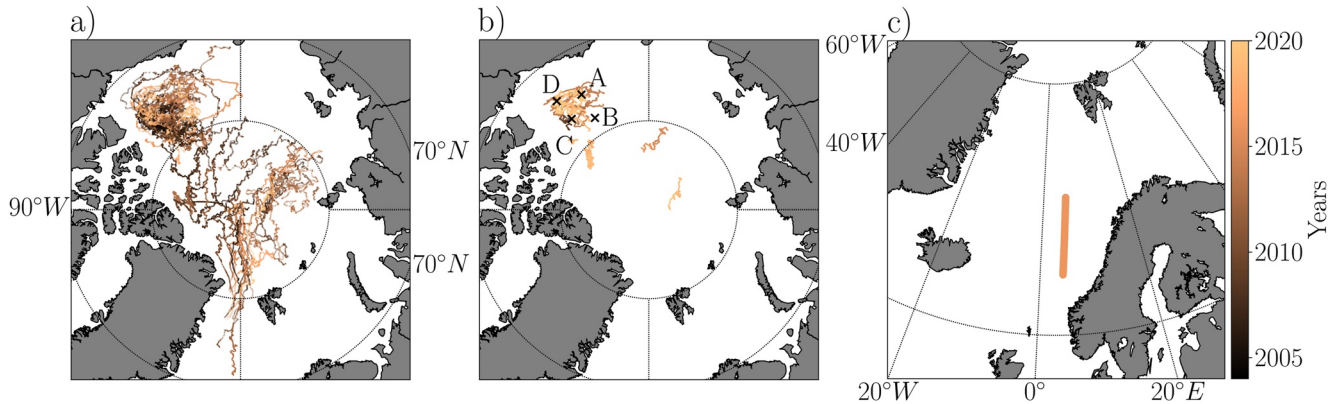


Figure 1. Maps showing the trajectories of (a) the ITP, (b) ITP-V and (c) the transect corresponding to the PS101 expedition, all colored by the year when data were collected. The mooring positions in the Canadian Basin are indicated with letters on (b).

2. Data

As part of the Beaufort Gyre Observing System (BGOS, <https://www2.who.edu/site/beaufortgyre>; Proshutinsky et al., 2009), up to four moorings have been deployed and maintained in the Canadian Basin since August 2003 (A, B, C, D, see Figure 1b). At the time of the analysis, data were available until September 2018. An upward-looking Acoustic Doppler Current Profiler (ADCP) is mounted on the top of each mooring (except for mooring C), providing vertical profiles of horizontal ocean currents in the upper ~30 m. Note that the ADCP was installed on mooring D in 2005, and in 2010 for moorings A and B. Profiles are returned every hour, from which we compute daily means, in order to filter the higher frequency fluctuations (likely induced by tides or inertial motions). We use the processed data interpolated on a 2-m fixed vertical grid. In addition to the ADCP at the top, each mooring is equipped with a McLane Moored Profiler (MMP), which provides one-way vertical profiles of temperature, salinity and horizontal velocity between 50 and ~2,000 m, separated in time by intervals of 6 and 48 hr, alternately. Again, we use the processed data provided with a 2-m vertical resolution. Finally, sea ice draft on top of each mooring is measured by an Upward Looking Sonar (ULS). The final product is daily and has an associated uncertainty of 5–10 cm (Krishfield & Proshutinsky, 2006).

In addition to the mooring observations, we also make use of observations collected by ITP, that are available through the ITP Program (<http://www.who.edu/itp/>, Toole et al., 2011). An ITP is similar to an Argo float, albeit drifting with the sea ice floe on which it is installed rather than ocean currents. An ITP is composed of a surface buoy sitting on top of a sea ice floe, which supports a wire rope extending through sea ice and into the ocean, with a weight at the end to keep the wire vertical. The profiler climbs up and down along the wire and samples temperature, salinity, and pressure from ~7 m down to 750 m, with a nominal 1 Hz sampling rate (corresponding roughly to a vertical resolution of 0.25 m). Each ITP returns between 2 and 6 vertical profiles per day. In addition, some ITPs are equipped with a velocity sensor and return horizontal velocity (ITP-V; Cole et al., 2015). Between 2004 and 2019, 121 ITPs have been deployed over the Arctic Basin, providing ~136,000 profiles (Figure 1a), while 13 ITP-V provided 40,791 profiles including velocity (Figure 1b). In the present analysis, we use data from 103 ITPs that were fully processed (Level 3) and provided on a 1-m vertical resolution grid. The data from the additional ITPs are only processed to Level 2 and are provided on a 2-m vertical resolution grid. Throughout our analysis, we have checked that our results are not biased by the level of processing of our data set. In particular, we only use data processed at Level 3 in the spectra analysis presented in Sections 3 and 4.

Data from the Thermosalinograph (TSG) mounted on the R/V POLARSTERN gathered during the PS101 expedition in the Nordic Seas in October 2016 are also examined (Boetius & Rohardt, 2017). The transect used here is roughly a straight line in the Norwegian Sea (Figure 1c). Temperature and salinity were measured at 11 m depth with a 10-min sampling interval.

Last, we make use of the sea ice concentration data set distributed by the EUMETSAT Ocean and Sea Ice Satellite Application Facility (OSISAF, product OSI-401-b). The product is distributed as daily fields since 2016 on a regular grid with a horizontal resolution of 10 km (Tonboe et al., 2017).

Throughout the study, we use the Gibbs SeaWater (GSW) Oceanographic Toolbox of TEOS-10 adapted for Python (<http://www.teos-10.org/>) to compute density and potential density from conservative temperature and absolute salinity, the freezing point temperature as well as dynamical height and geostrophic velocity from in situ profiles of temperature and salinity.

3. (Sub)mesoscale Dynamics in the Surface Layer

We start by providing a description of the ocean dynamics at mesoscale and submesoscale in the surface layer of the Arctic Ocean, for the seasonal and perennial ice zone separately, and explore their time and space variations, which are examined in conjunction with the variations in sea ice conditions.

3.1. The Seasonal Ice Zone

We first compute the temporal variability of the kinetic energy (KE) in the seasonal ice zone of the Canadian Basin, using the BGOS moorings located in this region. Using the ADCPs mounted on moorings A, B and D, the KE time series averaged over the top 30 m (Figure 2b) is estimated as in Cassianides et al. (2021):

$$KE = \int \left(\frac{1}{2} (u_o^2 + v_o^2) dz \right) / h \quad (1)$$

with u_o and v_o the two components of the horizontal ocean velocity and h the layer thickness (30 m here). Figure 2a also shows the evolution of the sea ice draft estimated from the ULS. There is a clear anti-correlation between sea ice draft and surface KE at all moorings. Sea ice draft evolves seasonally, with a maximum found in March–April around 2 m, and a minimum occurring in September that reaches 0 in some years but not all. KE is exhibiting a common behavior at all moorings: there is a very low background value all year long of about $1.5 \times 10^{-4} \text{ m}^2 \text{ s}^{-2}$, corresponding to the very weak mean currents found in the center of the Beaufort Gyre where the moorings are located (Regan et al., 2019), contrasting with large peaks (reaching around $1 \times 10^{-2} \text{ m}^2 \text{ s}^{-2}$) visible during summer. These events, associated with high KE sustained over a few days, are the signature of the passage of eddies in the surface layer (Cassianides et al., 2021). The most energetic events occur during summer 2012, 2015, 2016 and 2017, with values reaching up to $3.5 \times 10^{-2} \text{ m}^2 \text{ s}^{-2}$. This also corresponds to periods when the sea ice draft is zero. In contrast, during summer 2013 and 2014, when sea ice draft remains nearly 1 m thick at the end of the melting season, peaks in KE are weaker and less numerous. Lower levels of KE are logically found in winter, when the presence of thick sea ice insulates the surface from atmospheric forcing, dissipates existing eddies through sea ice friction (Ou & Gordon, 1986) and tends to make the ocean surface layer baroclinically stable (Meneghello et al., 2021). Overall, at first order, the time and space variations in KE in the seasonal ice zone, and in particular its seasonal cycle, are driven by the variability of the sea ice cover.

3.2. The Perennial Ice Zone

Mooring observations in years when the moorings remain under sea ice all year long suggest that the energy remains small under the sea ice pack. Unfortunately, the nature of the moored instruments that record time variability at a given location (for which a theoretical framework is lacking to interpret the variations in potential energy; e.g., Ferrari & Wunsch, 2010), as well as the lack of hydrographic observations in the surface layer, render the BGOS mooring observations unsuitable to investigate further how the energy is shared across scales in the ice-covered Arctic. Instead, we use ITP observations of potential density under sea ice to estimate horizontal wavenumber (k) spectra of the potential density variance. Note that computing these spectra are equivalent to examining the variability in potential energy. Similar analysis has been performed previously by for example, Timmermans et al. (2012) in order to examine the small scale processes important for the restratification of the surface layer, albeit only considering observations from a single ITP over 5 months.

Here we select data at 10 m from 27 ITPs spread across the Arctic. We select transects made in winter (November, December, January and February) and summer (June, July, August and September), in order to investigate the potential influence of seasonality. The two seasons are thus roughly corresponding to the sea ice freezing and melting seasons, respectively, meaning that the buoyancy forcing at the ocean surface has a different sign between the two seasons. Different definitions for the seasons were tested but do not affect our results qualitatively.

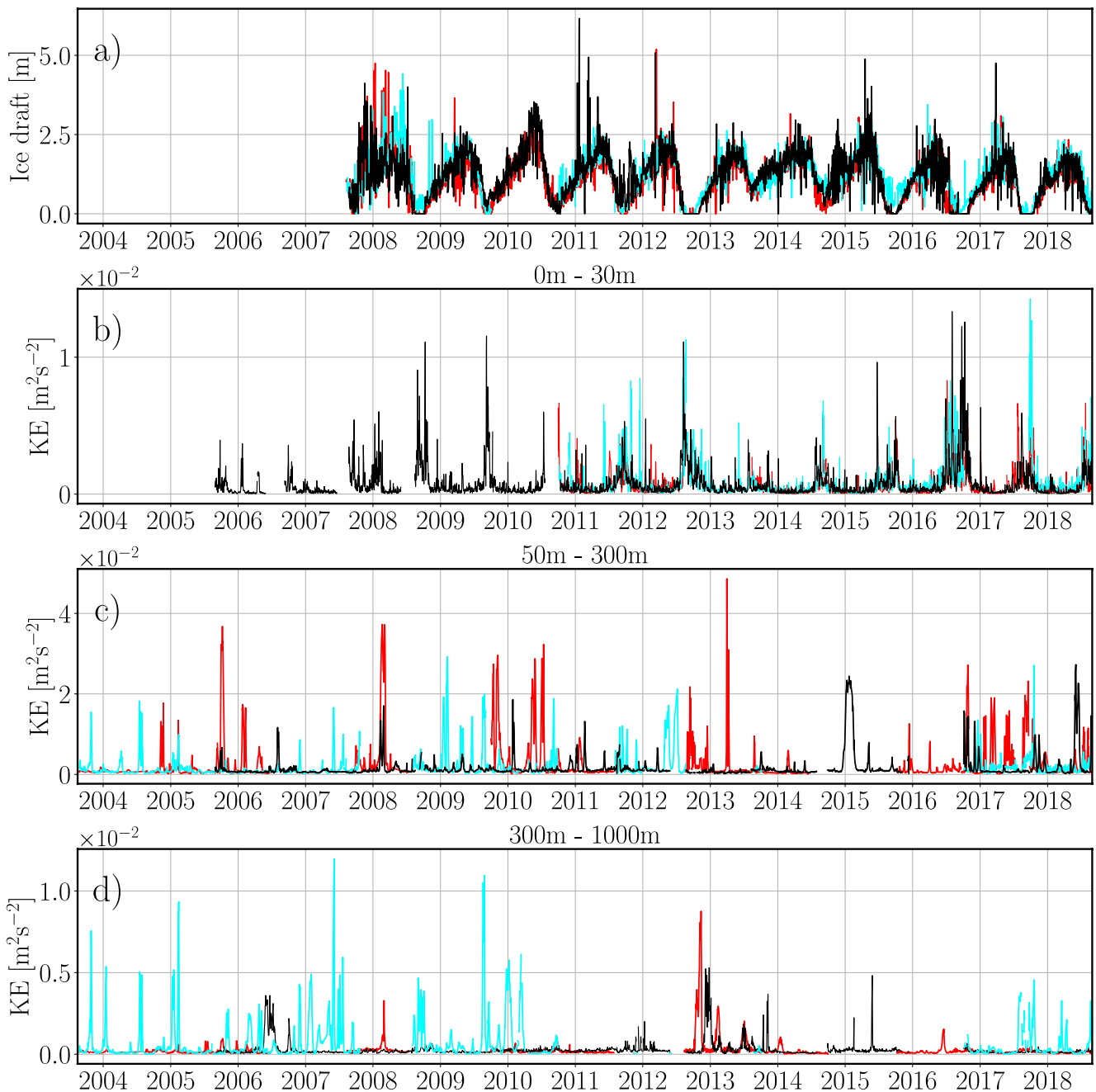


Figure 2. Time series of (a) sea ice draft and kinetic energy in (b) the surface layer (0–30 m depth), (c) the halocline layer (50–300 m depth) and (d) the Atlantic Water layer (300–1,000 m depth) estimated for the BGOS moorings A (red), B (cyan) and D (black). The time series shown in (a) and (b) have a daily resolution, while the ones in (c) and (d) have an alternating time resolution of 6 and 48 hr.

Regarding the sampling period of each instrument, a given ITP can provide data for one season only, or for both seasons. Some ITPs even cover two winters or two summers. Generally, ITPs drift faster ($\mathcal{O}(0.1 \text{ m s}^{-1})$) than the evolution of the Arctic mesoscale features, that are mostly advected by the weak background flow ($\mathcal{O}(0.03 \text{ m s}^{-1})$) on average at the mooring position, although this estimate may not be fully representative of the full basin where the ITPs are drifting). It means that the spectra analysis should allow us to examine the dynamics at mesoscale (length scales between R_d and 100 km), following the methodology developed by Timmermans et al. (2012) and applied to a subset of our observational data set. We acknowledge, however, that the difference in speed is not an order of magnitude, meaning that the ITPs sample not only the spatial variability of the eddy

field but also the temporal variability to some extent. For length scales smaller than R_d , we also anticipate that internal waves may significantly contribute to the variations in density, aliasing the signal and making it difficult to distinguish from these driven by the presence of submesoscale structures. Since all ITPs do not drift at the same speed and perform different number of profiles per day, the distance they travel (and thus the spatial resolution) between two consecutive profiles differ between them. Indeed, the distribution of the distance between two consecutive profiles shows that more than 70% of the values are below 3 km. The density profiles are thus interpolated on a regular 3-km grid. Note that our results are not sensitive to the choice of a finer grid (1 or 2 km). We apply a Hanning window to each density field to reduce side-band leakage effects due to the signal truncation (Thomson & Emery, 2014), and then a Fourier transform to get a spectrum. At this stage, each spectrum has a different length as each ITP travels a different distance during a season. In order to average the spectra, we create a common grid for each season and at each depth, limited by the shortest distance traveled (216 km for ITP 9). For each mean spectrum, we also compute the confidence interval at 95% with a chi-square distribution, taking into account that each individual spectrum has two degrees of freedom (the real part and the imaginary part). Finally, we estimate the best-fit slope in loglog space for the mesoscale range, between R_d and $10R_d$ (considering a constant R_d of 10 km).

The average across all the available spectra is shown on Figure 3a, along with all the individual spectra (shown as thin and transparent lines). The spectra are colored per season, in order to detect any potential seasonality. The best-fit slopes estimated between R_d and $10R_d$ for the seasonal means are -2.3 ± 0.03 and -3.0 ± 0.02 for summer and winter, respectively, and the level of energy is overall slightly higher at mesoscale in summer than in winter. We can compare them to the theoretical slopes $k^{-5/3}$ expected for the surface quasi-geostrophic dynamics (Blumen, 1978; Callies & Ferrari, 2013), commonly found at the surface where submesoscale features are generated from fronts, mixed layer instabilities and stirring from mesoscale structures (e.g., Callies et al., 2016; McWilliams, 2016). In the interior of the ocean, where turbulence arises from baroclinic instabilities fueled by potential vorticity anomalies, a quasi-geostrophic regime is most commonly found (Charney, 1971), characterized by a density spectrum with a slope steeper than k^{-3} (Charney, 1971; Klein et al., 2008). Here, despite looking at the surface, the mean spectra are steeper than one would expect from the surface quasi-geostrophic dynamics, suggesting a low energy at mesoscales, more consistent with a quasi-geostrophic turbulence scaling. The steep winter slope, in particular, is similar to the scaling found by Timmermans et al. (2012) estimated from data of a single ITP drifting in the Canadian Basin in winter 2009–2010, who further speculated that the steeper slope could be the result of the shear from ice-ocean stress suppressing submesoscale instabilities. We note that the frequency spectra are usually less steep than the wavenumber spectra (Arbic et al., 2012; Ferrari & Wunsch, 2010), so that the non synoptic sampling of the eddy field by the ITP would tend to make spectra less steep, not steeper than theoretical wavenumber spectra.

The seasonality of the spectra scaling is also striking, as it is at odds with what was observed in the open ocean, for example, in the western North Atlantic, where the submesoscale flows are much stronger in winter than in summer (Callies et al., 2015). Building on the hypothesis put forward by Timmermans et al. (2012), the seasonality found in the mean spectra could be driven by the sea ice conditions, with thick and less mobile winter sea ice conditions being more efficient at damping surface instabilities than summer conditions. To test this hypothesis, we extract two pairs of individual spectra (shown in the background on Figure 3a), and examine the sea ice conditions corresponding to these spectra (Figure 4). We first look at the case of two ITPs drifting in the same region north of Fram Strait in summers 2008 and 2013 (Figures 4a and 4b). The sea ice conditions are similar in both cases, with a mean concentration around 94%, a mean drift close to 0.1 m s^{-1} , meaning that any potential difference between the spectra is not arising from different sea ice drift that directly determine the sampling frequency. Despite this, the spectra estimated from the two ITPs are very different, with slopes of -2.1 in one case and -3 in the other. In both cases, we have checked that the ITPs are not crossing a coherent vortex. Similarly, we also compare the spectra estimated from two ITPs drifting in the Canadian Basin (north of the Canadian Arctic Archipelago) in winters 2005–2006 and 2007–2008 (Figures 4c and 4d). Again, despite similar conditions along the two trajectories (with more than 97% concentration and a drift oscillating around 0.1 m s^{-1}), the two spectra are very different, with slopes of -2.4 and -3.2 . These results suggest that the distribution of surface energy among scales is not solely determined by the sea ice conditions, the location nor the season considered. We acknowledge, however, that given the large spread between individual spectra shown in Figure 3a, examining only 4 individual spectra might not allow us to draw robust conclusions and to fully rule out the impact of the variations in sea ice conditions on the surface energy distribution. This is even more true as ITPs are, by design, only sampling a small

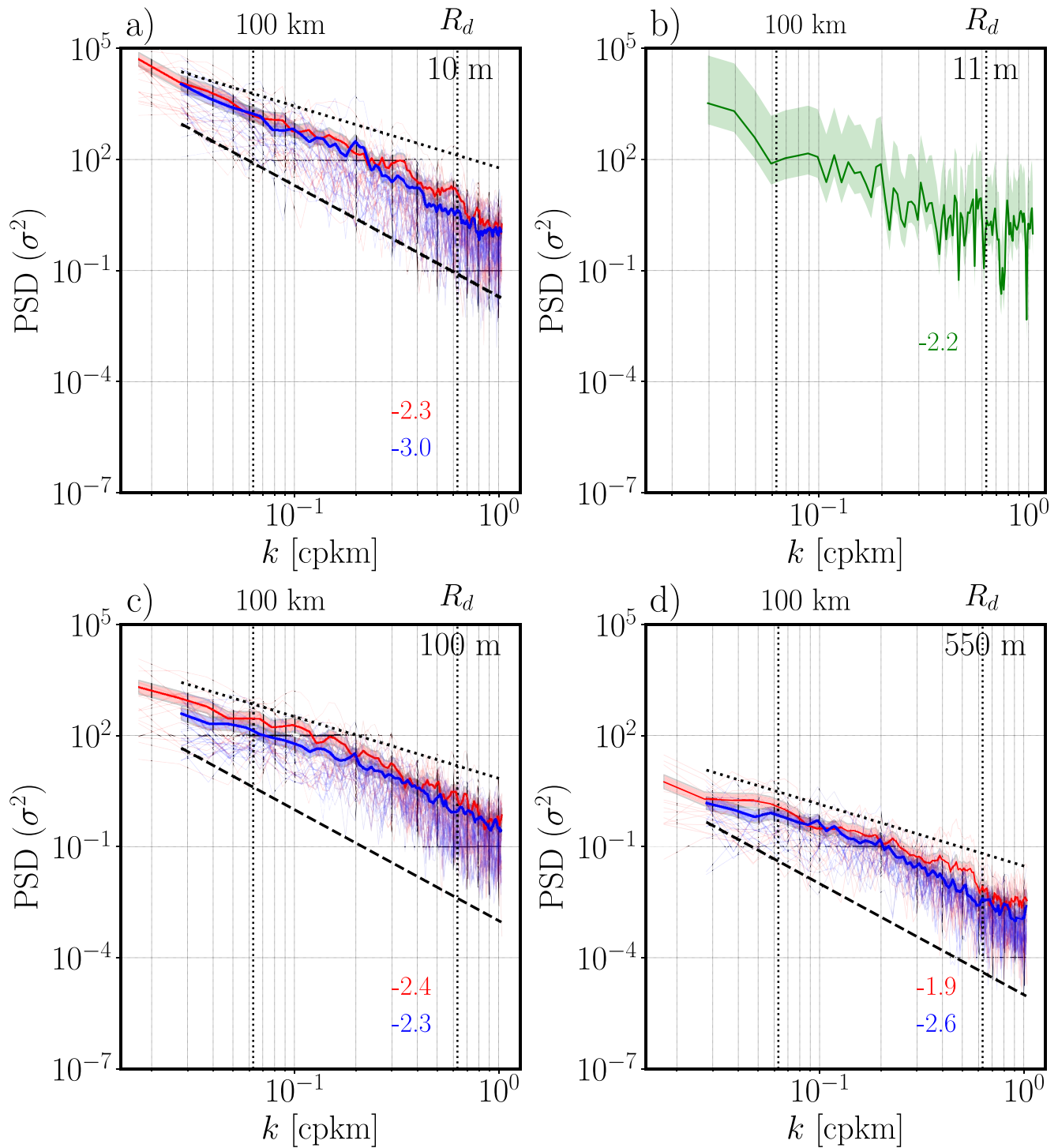


Figure 3. Wavenumber spectra of potential density variance (σ^2 in $\text{kg}^2 \text{m}^{-6}$) at (a) 10 m from ITP, (b) 11 m from the PS101 expedition, (c) 100 m from ITP and (d) 550 m from ITP. ITP trajectories are shown on Figure 5d. Spectra are shown in red for summer (defined as June–September) and blue for winter (November–February). The thick lines represent the average for each season and spectrum from each individual transect are shown in transparency. The light shadings around the mean spectra indicate the 95% confidence intervals. The mesoscale range is indicated as R_d – $10R_d$, with $R_d = 10$ km. The slopes of the seasonal mean spectra estimated in this range are indicated in colors. References with slopes of $-5/3$ (black dotted line) and -3 (black dashed line) are also indicated.

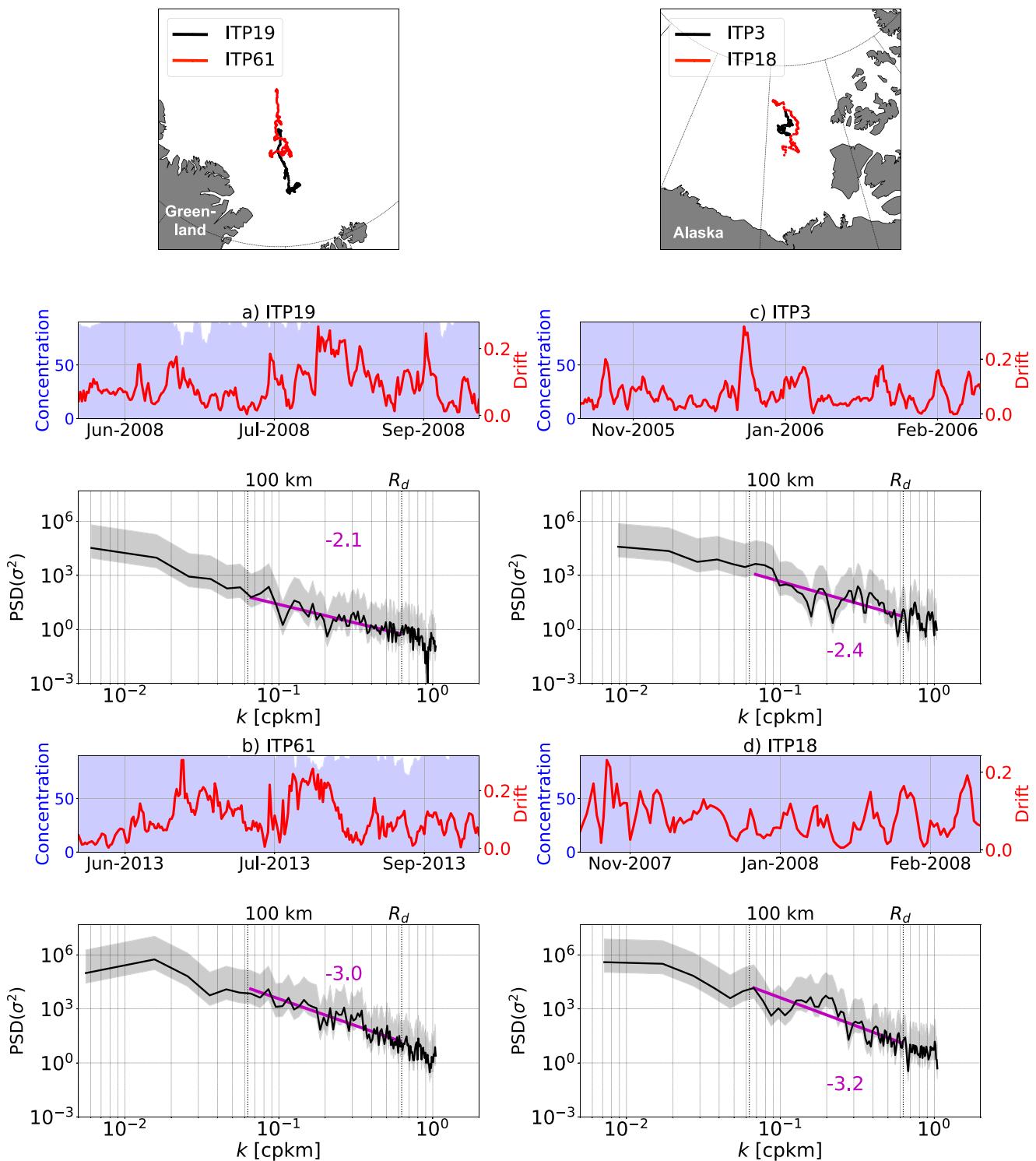


Figure 4. Wavenumber spectra of the potential density variance (σ^2 in $\text{kg}^2 \text{m}^{-6}$) at 10m depth estimated from (a) ITP 19 in summer 2008 in the Eurasian basin; (b) ITP 61 in summer 2013 in the Eurasian basin; (c) ITP 3 in winter 2005–2006 in the Canadian basin and (d) ITP 18 in winter 2007–2008 in the Canadian basin. The light shadings indicate the 95% confidence intervals. The mesoscale range is indicated as R_d-10R_d , with $R_d = 10$ km. The slopes of the spectra estimated in this range are indicated in magenta. The time series of the sea ice concentration (in blue, estimated from OSISAF and interpolated along the ITP trajectory) and the sea ice drift (in red, estimated based on the consecutive position recorded by the ITP) along the considered ITP trajectory are indicated on the top maps for the Eurasian (left) and Canadian Basin (right).

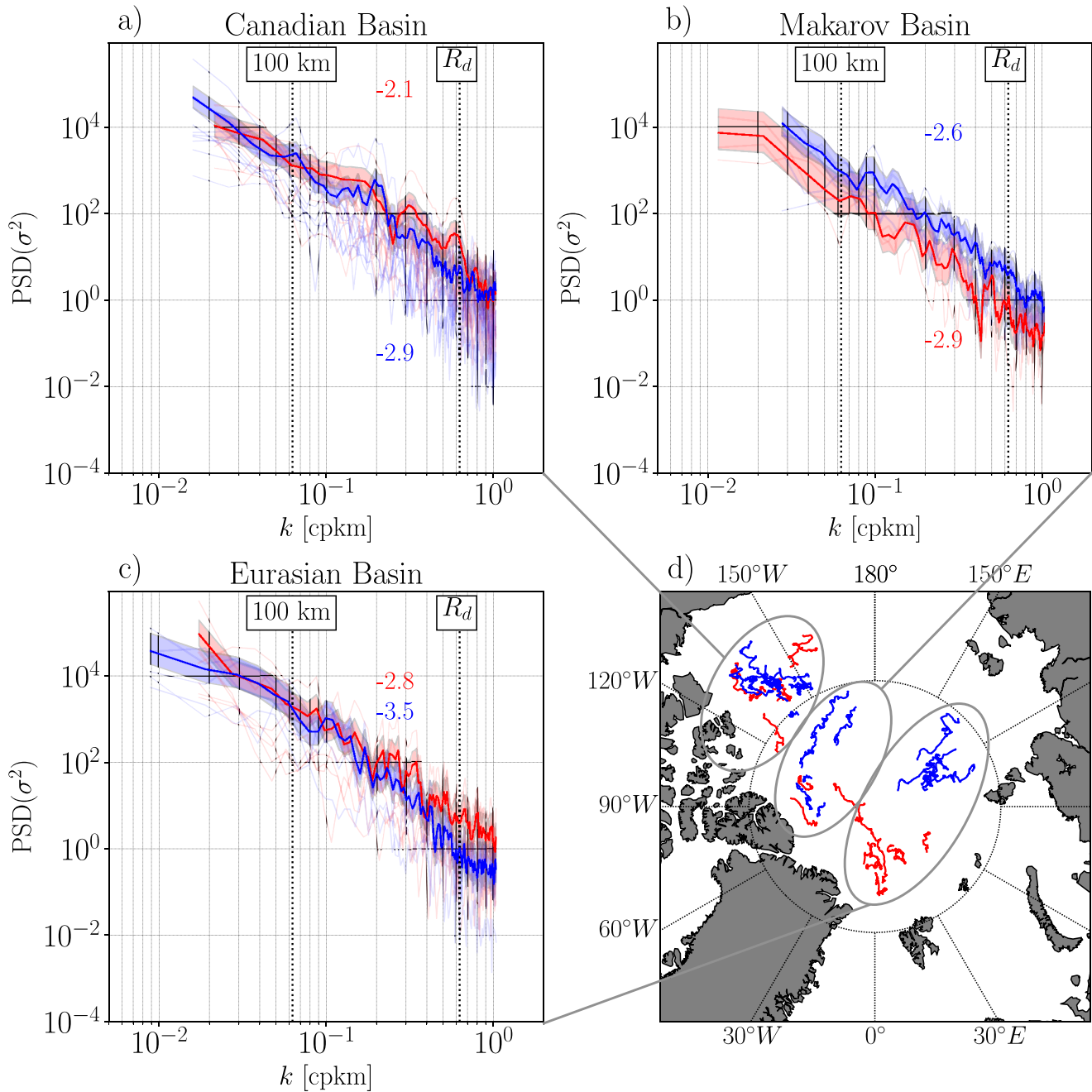


Figure 5. Wavenumber spectra of the potential density variance (σ^2 in $\text{kg}^2 \text{m}^{-6}$) at 10m from ITP for summer (red, June–September) and winter (blue, November–February), for different regions of the Arctic Basin, as indicated by the gray circles on the map (d). Individual spectra from each ITP are plotted in transparency and the thick lines represent the mean for each season. The light shadings indicate the 95% confidence intervals. The mesoscale range is indicated as R_d – $10R_d$, with $R_d = 10$ km. The slopes of the spectra estimated in this range are indicated in colors. The trajectories of ITP are indicated on the map and colored by season.

range of the sea ice conditions (corresponding to thick and concentrated sea ice conditions), and so the data set used here is not capturing the full extent of the seasonality in sea ice conditions.

To exemplify a possible impact of sea ice on the surface dynamics, we further compare all our spectra corresponding to sea ice conditions found in the pack (Figure 3a) to the spectrum obtained from the data of the PS101 cruise, that took place in the ice-free Norwegian Sea in October 2016 (Figure 3b). We select a section of about 638 km performed over 18–20 October 2016 and interpolate the density field at 11 m depth on a 3-km resolution grid before performing the analysis, consistently with the processing of the ITPs (although we acknowledge that

the transect was performed much faster than the drift of any ITP). Overall, the level of energy along this transect is similar to the level found under sea ice. The slope of the spectrum scales as $k^{-2.2}$, similar to what can be found under sea ice, at least in summer. This seems, once again, to be in contradiction with the hypothesis that the presence of sea ice damps the development of small-scale dynamics in the surface layer. Yet, as emphasized just previously, the representativeness of a single spectrum might be very limited. Indeed, Timmermans and Winsor (2013) used glider data in the ice-free Chukchi Plateau and found a k^{-3} scaling, while Mensa et al. (2018) found a spectrum scaling as k^{-2} when performing a similar analysis on TSG data gathered in summer 2016 in the ice-free Beaufort Sea, similar to what we estimate for the data from PS101 cruise. In addition to the limitations arising from the interpretation of individual spectra, the contrasted values might also hint at some geographical differences that could arise from the different stratification or mixed layer conditions found in the different parts of the Arctic (Peralta-Ferriz & Woodgate, 2015). Indeed, when considering different surface stratification, Callies and Ferrari (2013) (their figure 4) found that the theoretical slope of the density spectra can differ widely from the canonical $k^{-5/3}$ scaling.

To evaluate if the spread in the spectra could indeed arise from geographical differences, we group the different spectra per region (Figure 5). The choice of the three regions was made as the best compromise to obtain the best coverage and to allow us to examine seasonality within these regions when possible. Starting by looking at the spectra obtained from the ITPs drifting in the Canadian Basin, we find a similar behavior to what was found for the Arctic average (Figure 3a), with similar slopes and a steeper spectrum in winter (-2.9 ± 0.02) than in summer (-2.1 ± 0.01). Yet, this apparent seasonality, with more energy at smaller scales in summer is in stark contrast with what is found in the Makarov Basin. There, the slopes of the seasonally averaged spectra are very close (with a scaling of $k^{-2.6}$ and $k^{-2.9}$ in winter and summer, respectively), in line with the slope predicted from quasi-geostrophic theory. In this region, the sea ice conditions are most likely exhibiting little seasonality, while in the Canadian Basin, ITPs drift closer to the sea ice edge and might thus sample oceanic conditions forced at the surface by more diverse sea ice conditions depending on the season. When considering the Eurasian Basin, the ITP coverage is too sparse to obtain estimates for different seasons in all regions. Instead, we consider all the data available in the eastern side of the basin in winter, and obtain a very steep mean spectrum (with a slope scaling as -3.5 ± 0.04 , and an absolute value of the σ^2 variance weaker than in other regions), suggesting that in this region, the energy at mesoscale is very low. North of Fram Strait, when clustering all the spectra available for summer, the slope of the spectrum scales as -2.8 ± 0.05 , suggesting this time more energy at mesoscale but a weaker submesoscale dynamics. Again, as in the three regions, the ITP trajectories are not identical amongst seasons (and very distinct in the Eurasian Basin), we emphasize again here that part of the differences in our seasonal estimates may arise from regional differences of the ocean conditions.

Overall, we could not detect regions, seasons or environmental conditions with clear and contrasted dynamical regimes. There are some hints of some sort of seasonality, suggesting that some submesoscale turbulence might develop in the surface of some regions during summer, when sea ice is less of a barrier between the ocean and the atmosphere and when the sea ice stress at the surface weakens. This seasonality contrasts with the typical open ocean dynamics, where submesoscale turbulence tends to intensify in winter (Callies et al., 2015; Thompson et al., 2016), but also with what was found in the Antarctic MIZ, where the submesoscale flows were also observed to intensify in winter (Biddle & Swart, 2020). Yet, one might note that this intensification was suggested to be a response to the development of sea ice leads, which, in the Arctic, might occur more predominantly in summer. Further, using observations from gliders in the Antarctic MIZ, Giddy et al. (2021) reveal that submesoscale turbulence can be triggered at small scale surface fronts resulting from summer sea ice melt, a mechanism that might also be at play in the Arctic. Under the sea ice pack, most spectra indicate a lack of energy at submesoscales, in line with the results of Mensa and Timmermans (2017) and Shrestha and Manucharyan (2022) based on an idealized process model at very high resolution. Maybe more importantly, our analysis highlights the risk of drawing conclusions from a small data set, such as one ITP, as has been done in previous studies. Indeed, it is clear from the spread between all our spectra (Figure 3a) that one can find a spectrum with basically any slope, regardless of the region or the sea ice conditions (Figures 4 and 5).

4. (Sub)mesoscale Dynamics in the Subsurface Layer

We now turn our attention to the turbulence in the interior of the Arctic Basin. Observations have revealed the existence of a subsurface intensification in KE, with no significant seasonal variations (e.g., Manley &

Hunkins, 1985). This subsurface maximum is the signature of eddies formed by baroclinic instabilities and shielded from sea ice friction by a peak of stratification at the base of the surface layer (Meneghello et al., 2021). This suggests that, at depth, the impact of the presence of sea ice on the levels of turbulence might be very limited. This section aims at testing this hypothesis based on the analysis of available observations.

4.1. The Seasonal Ice Zone

Here we start again by estimating the variability of KE in the seasonal ice zone of the Canadian Basin, based on the observations from the MMP mounted on 3 of the BGOS moorings. KE is estimated in the halocline (50–300 m, Figure 2c) and in the Atlantic Water layer (300–1,000 m, Figure 2d) based on Equation 1. Note that MMP does not sample continuously above 50 m, so there is a gap with our surface layer defined as the top 30 m.

The background KE found at depth at the 3 moorings is similar in magnitude to the background KE quantified for the surface layer in Section 3 (Figure 2b), with values of about $5.7 \times 10^{-4} \text{ m}^2 \text{ s}^{-2}$ in the halocline and $1.7 \times 10^{-4} \text{ m}^2 \text{ s}^{-2}$ in the Atlantic Water layer. Similar to the behavior found in the surface layer, KE at depth is also largely dominated by energetic pulse-like events, reaching as high as $2.5 \times 10^{-2} \text{ m}^2 \text{ s}^{-2}$ and $7 \times 10^{-3} \text{ m}^2 \text{ s}^{-2}$ in the halocline and the Atlantic Water layers, respectively, with a larger number of pulses found in the halocline layer. Yet, in stark contrast to the surface layer, KE in the subsurface layer varies independently from the variability in the sea ice draft (Figure 2a), and thus does not exhibit any seasonality, in line with the finding of Meneghello et al. (2021). We note, however, that the lack of seasonal cycle in KE at depth could depend on the region considered, even beyond the seasonal ice zone. Indeed, based on results from a regional Arctic model at ~ 1 km resolution, Wang et al. (2020) suggest that KE in the interior exhibits a seasonal cycle over the Eurasian and Alaskan continental slopes, but not in the Beaufort Sea (in line with our mooring observations). Further, von Appen et al. (2022) reveal that in large parts of the Arctic, seasonal and interannual variability of the current might contribute significantly more to the mean KE than EKE. Thus, there might be some spatial and temporal variability unrelated to the sea ice conditions, that we explore in the following section.

4.2. The Perennial Ice Zone

We now return to ITP observations that sample potential density under the sea ice pack. Following the method previously presented, we use data from 27 ITPs to estimate wavenumber spectra of potential density variance (averaged again per season) at 100 m (in the halocline; Figure 3c) and 550 m (in the Atlantic Water layer; Figure 3d).

First, the comparison of the mean spectra at different depths reveals that the variance in potential density (and thus potential energy) decreases with depth, with spectra at 550 m being roughly three and two orders of magnitude weaker than at 10 and 100 m, respectively. Second, similarly to the surface layer the energy is, on average, slightly stronger in summer than in winter. When computing the best fit slope, we find that the two mean seasonal spectra exhibit similar slopes at 100 m (close to -2.4), while at 550 m, the slope is flatter in summer (-1.9 ± 0.04) than in winter (-2.6 ± 0.02), similar to the behavior found at the surface. Third, when looking at individual spectra, it is however clear that, similarly to the surface layer, one can find in the interior a large variety of spectra, with slopes varying between -1 and -4.2 . Here again, we could not find any significant clustering of the spectra when splitting up the spectra per region, season or sea ice conditions (not shown).

The spread amongst our spectra estimated in the halocline could explain the discrepancy with the results of Marcinko et al. (2015) and Timmermans et al. (2012). Indeed, based on a few transects across the Arctic, they both found spectra that are scaling very well with a k^{-3} slope, in line with what is expected for interior quasi-geostrophic turbulence over the mesoscale range. The picture we draw from our more extensive data set is more complex, and further analysis of the dynamics at play in the interior will be required in order to fully elucidate the mechanisms driving the energy distribution across scales. Our results, however, highlight that the sea ice conditions and their spatio-temporal variations appear to be only one of possible relevant mechanisms determining the variability of the small scale dynamics in the halocline, as also suggested by Marcinko et al. (2015). The small seasonality found in the Atlantic Water layer remains puzzling. In this layer, the thermohaline properties (and thus density) are lacking any seasonality in most of the basin away from the entrance of the Atlantic Water layer at Fram Strait (Lique & Steele, 2013). It is thus very surprising to find a seasonality in the slope of the spectra averaged across the basin (Figure 3d).

5. Local Eddy-Sea Ice Interactions

In Sections 3 and 4, we have provided a detailed description of the small scale dynamics in the different regions of the Arctic. We found that, while, in the surface layer, the presence of sea ice seems to dampen strongly the mesoscale flow, this is not the case at depth where the levels of energy at mesoscale are not affected by the presence of sea ice. Both at the surface and at depth, coherent eddies are largely dominating the variability in KE (Cassianides et al., 2021; Zhao et al., 2018), and as such, the interactions between these features and sea ice could potentially be important for understanding the interplay between ocean and sea ice. The goal of this section is thus to perform an eddy census in order to investigate the local interactions between eddies and sea ice.

5.1. Eddy Census

We first use the full ITP, ITP-V and BGOS mooring datasets to perform an eddy census over the period 2004–2019, expanding significantly the latest census performed by Zhao et al. (2016) (up to 2015). Our eddy detection is largely done by visual inspection. It is primarily based on the method of Zhao et al. (2014), although, here, an eddy is characterized by both (a) an isopycnal displacement and (b) a temperature or a potential vorticity (PV) anomaly instead of solely an anomaly of temperature as in Zhao et al. (2014). This allows us to detect eddies that are not associated with temperature anomaly in their core. PV is estimated as $\frac{f_0}{\rho} \left(\frac{\partial \rho}{\partial z} \right)$ with ρ the potential density and f_0 the Coriolis parameter, taken as the value at the North Pole ($f_0 = 1.45 \times 10^{-4} \text{ s}^{-1}$). Anticyclonic and cyclonic eddies are associated with a convex-shape and concave-shape isopycnal displacement, respectively, and the depth of the feature is taken as the depth of the maximum temperature or PV anomaly. When considering observations from ITP or ITP-V, we only detect an eddy when the instrument crosses the structure with a rather straight trajectory, as the anomaly in density could be the signature of a front or a meander otherwise. We then compare the characteristics of consecutive eddies sampled within a few days and remove any eddy sampled twice. We also require that a given eddy has a signature in a minimum of four consecutive profiles for both ITP and moorings. For ITP and their typical $\sim 2\text{--}3$ km distance between profiles, and given the typical R_d of ~ 10 km in the Arctic, it means that our detection should be able to capture both mesoscale and submesoscale eddies. When using mooring data, we assume that eddies are advected by a background flow of $\sim 0.03 \text{ m s}^{-1}$, corresponding to the mean weak background flow measured by the mooring in the halocline layer. Given the temporal sampling, four consecutive profiles across an eddy diameter thus correspond roughly to 12 km, meaning again that both mesoscale and submesoscale eddies can be sampled.

As our detection method is based on the analysis of temperature and salinity data, it cannot be applied to the top 50 m of the moorings (where temperature and salinity measurements are lacking). Based on ITP and ITP-V profiles, the shallowest eddies detected are centered at ~ 20 m. Above this depth, it often corresponds to the mixed layer where PV anomalies are too small to be detected.

Once an eddy is detected, we further estimate its radius when horizontal velocity data are available (i.e., for eddies detected from the mooring and ITP-V data sets). The eddy radius R_{eddy} is defined as half the distance between the two maximum azimuthal velocities U found on each side of the eddy, that we approximate to the maximum speed. This approximation relies on the assumption that the eddy center has passed through the mooring location, or that the ITP-V has drifted across the eddy center.

As a result, 505 eddies are detected (Figure 6), 103 from the moorings (Figure 6c), and 402 from the ITPs (51 in the Eurasian Basin and 351 in the Canadian Basin; Figure 6d). Among the 505 eddies, 14 are cyclones and 491 anticyclones.

The vast majority of the eddies have their core in the halocline, although some can be quite shallow (with a core between 20 and 50 m; Figure 7), corresponding to situations when the mixed layer is shallow as well. Among the detected features, we found 333 ones with an anomalously cold core, and only 45 with an anomalously warm core or no significant temperature anomaly (113 eddies). For the 14 cyclones, we do not detect any temperature anomaly. The properties of the water trapped in the eddy core can provide useful information on their region of formation (e.g., Pnyushkov et al., 2018). Figure 7 reveals that the core temperatures largely cluster close to the freezing point line, while the core salinities span a large range of values ($S \sim 28\text{--}35$ psu for the Canadian Basin and $S \sim 32\text{--}35$ psu for the Eurasian Basin). Temperatures close to the freezing point are suggesting that eddies were formed either at the surface under sea ice and then advected deeper to the halocline where they are mostly detected, or at depth in the Canadian Basin within the layer encompassing Winter Pacific Water, characterized by salinity of $\sim 32\text{--}33$ psu and temperatures close to the freezing point (Shimada et al., 2005). It means that eddies with core salinity fresher than 32 psu are

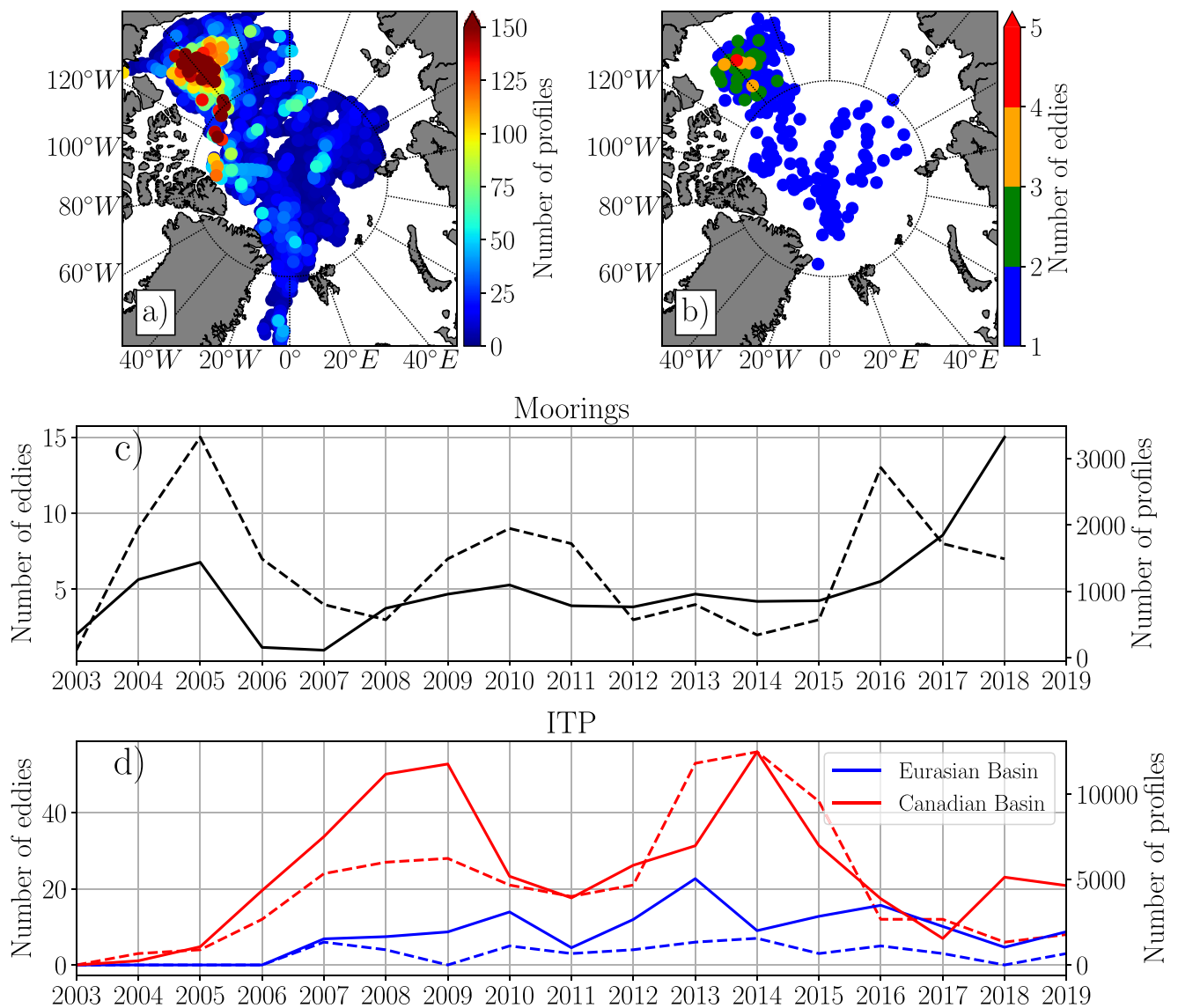


Figure 6. Spatial distribution of (a) the number of profiles and (b) position of the core of all the eddy detected by ITP-(V), per $0.5^\circ \times 0.5^\circ$ bins from all ITP-(V). Time series of (c) the number of profiles (solid line and right y-axis) and eddies detected (dashed line and left y-axis) from the moorings data set; and (d) the number of profiles (solid lines and right y-axis) and eddies detected (dashed lines and left y-axis) in the Canadian (red) and Eurasian (blue) basins from the ITP-(V) data set.

most likely formed at the surface. On average, the surface waters are fresher in the Canadian Basin ($S \sim 28\text{--}35$ psu) than in the Eurasian Basin ($S \sim 32\text{--}35$ psu), except for regions on the shelves close to river mouths, where salinity can be as low as 20 psu (Supply et al., 2020). As, in general, the cores of the eddies found on the Canadian side are mostly fresher than in the Eurasian side, it suggests that eddies are detected largely in the region where they were formed.

We also detect a significant number of eddies with no significant temperature anomaly in their core. Note that this type of eddy was not considered in the census made by Zhao et al. (2014) and Zhao et al. (2016), explaining partly the higher number of eddies captured by our analysis. These eddies are likely formed at depth in the interior of the Canadian Basin through baroclinic instabilities (Meneghello et al., 2021) and remain afterward in the same region, likely contributing to the equilibration of the Beaufort Gyre (Doddridge et al., 2019). It is thus useful to obtain a detailed description of their properties. From their census, Zhao et al. (2016) noted that the number of halocline eddies has doubled from 2005 to 2012 to 2013–2014, an increase that they attributed to the intensification of the Beaufort Gyre that occurred over the same period (Regan et al., 2020), rather than the increase in the number of profiles. Similarly, we find a large interannual variability in the number of eddies detected by our method, that is the largest for the eddies encountered by ITPs in the Canadian Basin (Figures 6c and 6d). The number of eddies detected in the Canadian Basin

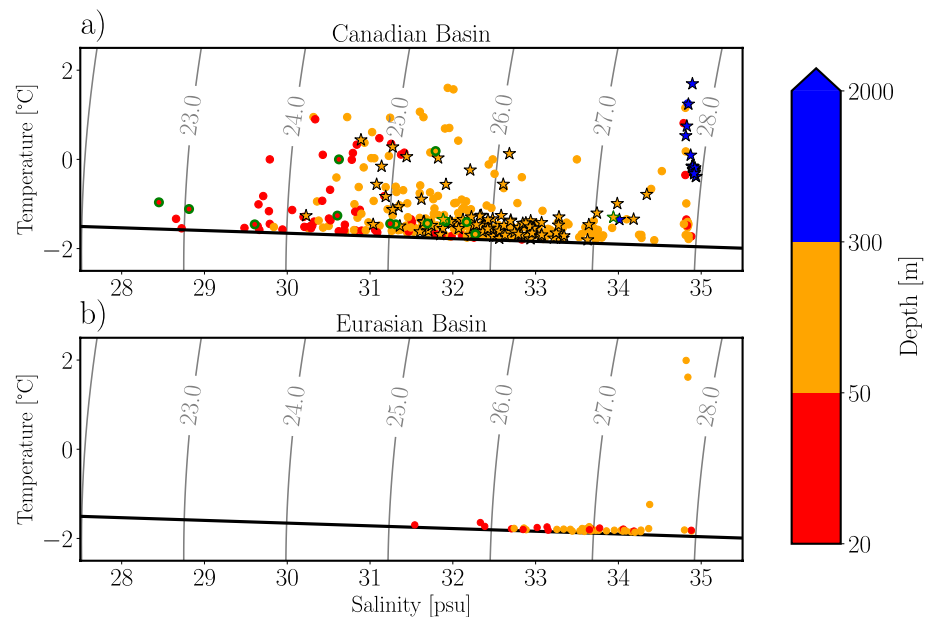


Figure 7. Temperature-salinity diagram of the properties found in the eddy cores in (a) the Canadian Basin and (b) the Eurasian Basin. Each dot corresponds to an eddy, and is colored by the depth of the core. The stars indicate eddies detected at the moorings and circles with a green contour indicate the cyclones. Isopycnals are in gray. The thick black line indicates the freezing point line.

by ITP reaches its maximum in 2014, but this year also corresponds to a peak in the number of profiles in the region, where the sampling by ITP is the densest (Figure 6d). Overall, the large spatio-temporal variations in data coverage make it very hard to determine if changes in the number of detected eddies are resulting from changes in data coverage (Figure 6a) or changes of the number of eddies existing in the Arctic. Yet, Figure 6d suggests a strong correlation between the number of profiles in the Canadian Basin and the number of eddies detected in the region. Moreover, as we could not find an increase in the number of eddies without temperature anomaly, nor in the number of eddies captured by the moorings in the interior of the gyre (Figures 2 and 6), our results question the finding that the variations in the number of eddies in the Canadian Basin would be related with the intensification of the gyre. Instead, it is likely that the gyre spin up had resulted in an increase of the mean KE rather than the EKE (Regan et al., 2020).

We further comment on two interesting characteristics of our census. First, we could not find any significant seasonality in the number of eddies nor in their properties. This is not surprising as eddies are long-living features (from months to years; e.g., D'Asaro, 1988; Manley & Hunkins, 1985), which is likely buffering any potential seasonality in their generation. Yet, the lack of seasonality in the number of eddies at depth contrasts again with the seasonality in KE found at the surface in the seasonal ice zone (Figure 2b), reinforcing the idea that eddies at depth can evolve freely without being dissipated by the seasonally varying sea ice friction (Ou & Gordon, 1986). Second, we note that our eddy field is mostly anticyclonic, with the detection of 14 cyclones and 491 anticyclones, in line with the findings of previous observational and modeling studies focusing on the halocline (Manley & Hunkins, 1985; Wang et al., 2020; Zhao et al., 2016). This however contrasts with the analysis of Pnyushkov et al. (2018) who found an equal number of cyclones and anticyclones passing by a mooring in the Laptev Sea, and the results of Kozlov et al. (2019) who found that, at the surface of the Arctic ice-free regions, cyclones are twice as numerous as anticyclones. This asymmetry in the number of cyclones and anticyclones may arise from a known deficiency of any detection method based on isopycnal displacement (Giulivi & Gordon, 2006) or a possible shorter life of cyclones compared to anticyclones (Carton et al., 2014), but it might also be related to some Arctic-specific physical mechanisms that tend to promote the generation and propagation of subsurface anticyclones at ice-covered surface fronts (Brannigan et al., 2017).

In order to gain some insights on the eddy dynamics, we further estimate some useful quantities when velocity measurements are available (Figure 8). Following D'Asaro (1988) and Manley and Hunkins (1985), eddy vorticity ζ can be scaled in cylindrical coordinates as $\frac{2U}{R_{eddy}}$. We assign a negative sign (respectively positive) to an anticyclone (respectively a cyclone). Finally, we estimate the Rossby number Ro as $\frac{U}{f_0 R_{eddy}}$. Eddies with Ro smaller than one are largely in geostrophic balance, while eddies characterized by $Ro \sim 1$ are often associated with submesoscale turbulence.

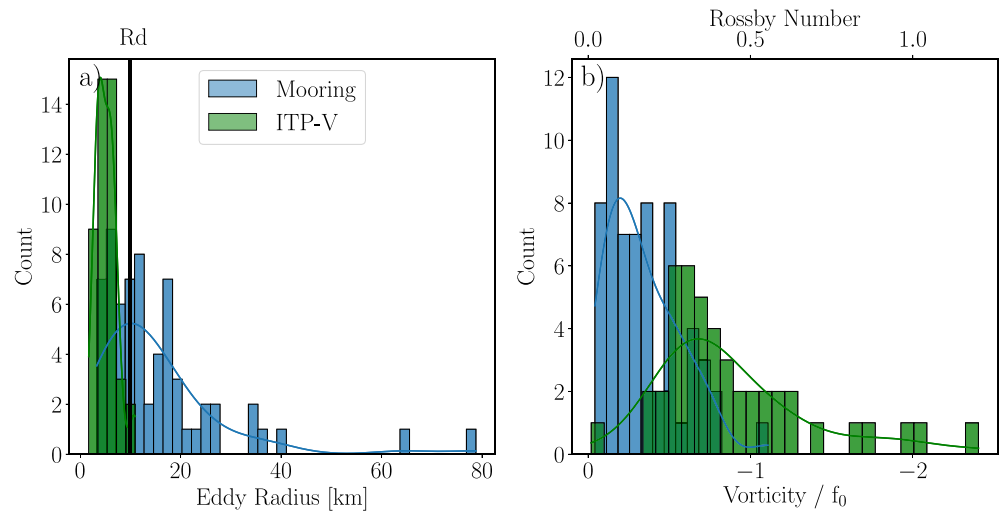


Figure 8. Probability density function of (a) radius, (b) vorticity (normalized by f_0) and Rossby number for the eddies captured by the moorings (blue) and the ITP-V (green). R_d is indicated in (a) as a vertical line.

Looking at the distribution of the eddy radius, there is a striking difference between the ITP-V data set on one side and mooring data set on the other side (Figure 8a). While eddies detected from mooring observations have a large variety of radius, spanning from 3 to 80 km (with a peak in the distribution around 10 km), ITP-V only captures small eddies, with radius between 3 and 10 km. Most of the eddies detected by ITP-V are smaller than the deformation radius R_d , and correspond to the SCV first identified in the central Beaufort Sea by D’Asaro (1988), although we note that the same structures were labeled as ‘mesoscale eddies’ by Zhao et al. (2014). The difference found in radius logically translates into differences in vorticity and Rossby number (Figure 8b). While moorings allow the detection of eddies with normalized vorticity ranging from -0.1 to -1 (and Ro between 0.05 and 0.5), SCV sampled by ITP-V tend to be characterized by larger normalized vorticity and Rossby number. The differences in scales and properties of the structures captured by our two datasets appear to be robust, as the number of sampled eddies is significant. Yet, it remains puzzling as both observing systems are sampling the same region (Figure 1b). Based on the analysis of mooring observations in the Eurasian side equipped with similar MMP and a similar sampling strategy (with profiles spaced by 6 and 48 hr, alternatively), Pnyushkov et al. (2018) found eddies with similar Rossby Number ($Ro < 0.1$), suggesting that larger and weaker eddies are preferentially observed by moored instruments of this kind, which may not be suitable to capture smaller scale features. Indeed, one needs to remember that ITP and mooring are returning observations of fundamentally different nature: while mooring provide time-varying observations at a fixed point (i.e., an eddy crosses the position of the mooring), an ITP drifts with sea ice faster than the ocean current (i.e., the ITP drift across an eddy). We hypothesize that this may be the reason for the discrepancy between the structures observed, although further analysis of for example, model fields that can be alternatively sub-sampled in time and space to mimic the instruments sampling would be required to fully elucidate this mismatch.

5.2. Potential Surface Signature in Sea Ice of the Subsurface Eddies

As mentioned in Section 1, previous studies have revealed that eddies and filaments can imprint their signature on sea ice through thermodynamical (Gupta et al., 2020; Horvat et al., 2016; Manucharyan & Thompson, 2017) and dynamical (Cassianides et al., 2021; Kozlov et al., 2020; Manucharyan et al., 2022; von Appen et al., 2018) processes. Yet, these analyses have three main limitations: (a) they are often based on results from idealized process models, (b) they only consider the potential signature of surface eddies and (c) they are limited to a few case study. Here, we aim to quantify the potential impact on sea ice of our numerous observed subsurface eddies.

First, the passage of a subsurface eddy at a given location could modulate the sea ice growth and melt rate (Gupta et al., 2020), by disturbing the stratification and modulating the local vertical heat flux (e.g., Lique et al., 2014). To quantify this impact, we use the ITP(-V) data set to estimate the mixed layer heat content as:

$$Q_{ML} = \rho_0 C_p \int (T_{ML} - T_f) dh \quad (2)$$

with ρ_0 a reference density ($1,027 \text{ kg m}^{-3}$), C_p the ocean specific heat capacity ($3,985 \text{ J kg}^{-1} \text{ K}^{-1}$), $(T_{ML} - T_f)$ the difference between the mixed layer temperature T_{ML} and the freezing point temperature in the mixed layer T_f and dh the thickness of the mixed layer. The mixed layer depth is estimated based on a threshold criterion of 0.1 kg m^{-3} (Peralta-Ferriz & Woodgate, 2015), compared against the first available measurements closest to the surface. In order to estimate the anomaly in mixed layer heat content associated with the passage of an eddy (ΔQ_{ML}), we assume that the average of Q_{ML} at the two eddy edges represents the background Q_{ML} , to which we subtract the value of Q_{ML} at the eddy center. Here we consider the edge as the average between the closest two profiles on each side of the eddy in which we do not detect a PV or temperature anomaly. ΔH_{ML} , corresponding to the anomaly in mixed layer depth associated with the passage of an eddy, is estimated with the same method. The anomaly in mixed layer heat content can be directly converted into an equivalent change in sea ice thickness (Davis et al., 2016):

$$\Delta H_{ice} = \left(\frac{\Delta Q_{ML}}{\rho_{ice} L_{ice}} \right) \quad (3)$$

where ρ_{ice} is sea ice density (900 kg m^{-3}) and L_{ice} the latent heat of fusion of sea ice ($3 \times 10^5 \text{ J kg}^{-1}$). ΔH_{ice} can be interpreted as the sea ice thickness that would have been melted or formed in response to the mixed layer heat anomaly induced by the passage of an eddy below the mixed layer.

The distributions of ΔH_{ML} , ΔQ_{ML} and ΔH_{ice} are shown on Figures 9a and 9b. Regardless of the type of eddy considered, the anomaly in mixed layer depth is in most cases a shoaling by a few tens of centimeters (with a mean distribution centered around 0.7 m; Figure 9a). ΔQ_{ML} is small and distributed around zero, with values spreading over both positive and negative small variations of $\pm 2 \times 10^7 \text{ J m}^{-2}$ (Figure 9b). It is surprising that even in the case of an eddy with a warm core (in red), there is no important change in the mixed layer heat content. The small variations in ΔQ_{ML} induce a small change in sea ice thickness, with a peak in the distribution at 0. In the vast majority of our observed eddies, the potential induced melt remains small compared to the total bottom melt observed in the ice pack over a typical melting season, estimated to be $\sim 50 \text{ cm}$ by Perovich and Richter-Menge (2015). The small impact on sea ice thickness might be due to the fact that the core of the majority of the eddies is close to the freezing point temperature, but also to the strong stratification at the base of the mixed layer that might prevent the transfer of heat upward, isolating sea ice from the thermodynamical impact of eddies. Although associated with errors, these calculations are the only way we could estimate of the thermodynamical impact of the eddy on sea ice. Indeed, some Ice Mass Balance (IMB) buoys were deployed on top of some ITP-V, providing direct in situ observation of sea ice thickness, but we could not find any data available when an eddy was detected. A few eddies stand out from our distribution, with value of ΔH_{ice} reaching as high as 5 cm (Figure 9b). We speculate that in specific conditions of stratification or eddy properties, the passage of eddies may contribute to the large spatial variations in sea ice bottom melt reported by Perovich and Richter-Menge (2015).

Second, subsurface eddies could impact sea ice dynamically. It is well known that subsurface eddies can have a signature in sea surface height (SSH; e.g., Chelton et al., 2011), as exemplified by the cases of meddies that have been associated to a local anomaly of 5–15 cm by Bashmachnikov and Carton (2012). If significant, SSH anomalies (and associated geostrophic velocities and vorticity) resulting from the propagation of subsurface eddies in the Arctic could represent a significant forcing for the sea ice momentum balance, and thus modulate the sea ice drift (Zhang et al., 1999) and vorticity (Cassianides et al., 2021). To quantify this potential impact, we compute the dynamic height (DH) at the surface following the relation:

$$DH = \int_{p_1}^{p_2} \frac{dp}{\rho} \quad (4)$$

with p the pressure, p_1 the pressure at the level of no motion chosen at 250 m depth (as most of the ITP-V do not have data below 250 m depth), and p_2 the pressure at the first available data point closest to the surface. Although being the best choice possible given the availability of our data, we do acknowledge that the currents at 250 m in the Canadian Basin, where most of the ITP-V are drifting, are most likely non zero, and so our estimate of DH (and the quantities derived from it) may be somewhat biased. The sensitivity of our results to this choice is discussed below. Note also that the calculation could not be performed for eddy detected in the mooring data, as temperature and salinity data are not provided between above 50 m depth, preventing us from estimating dynamic height.

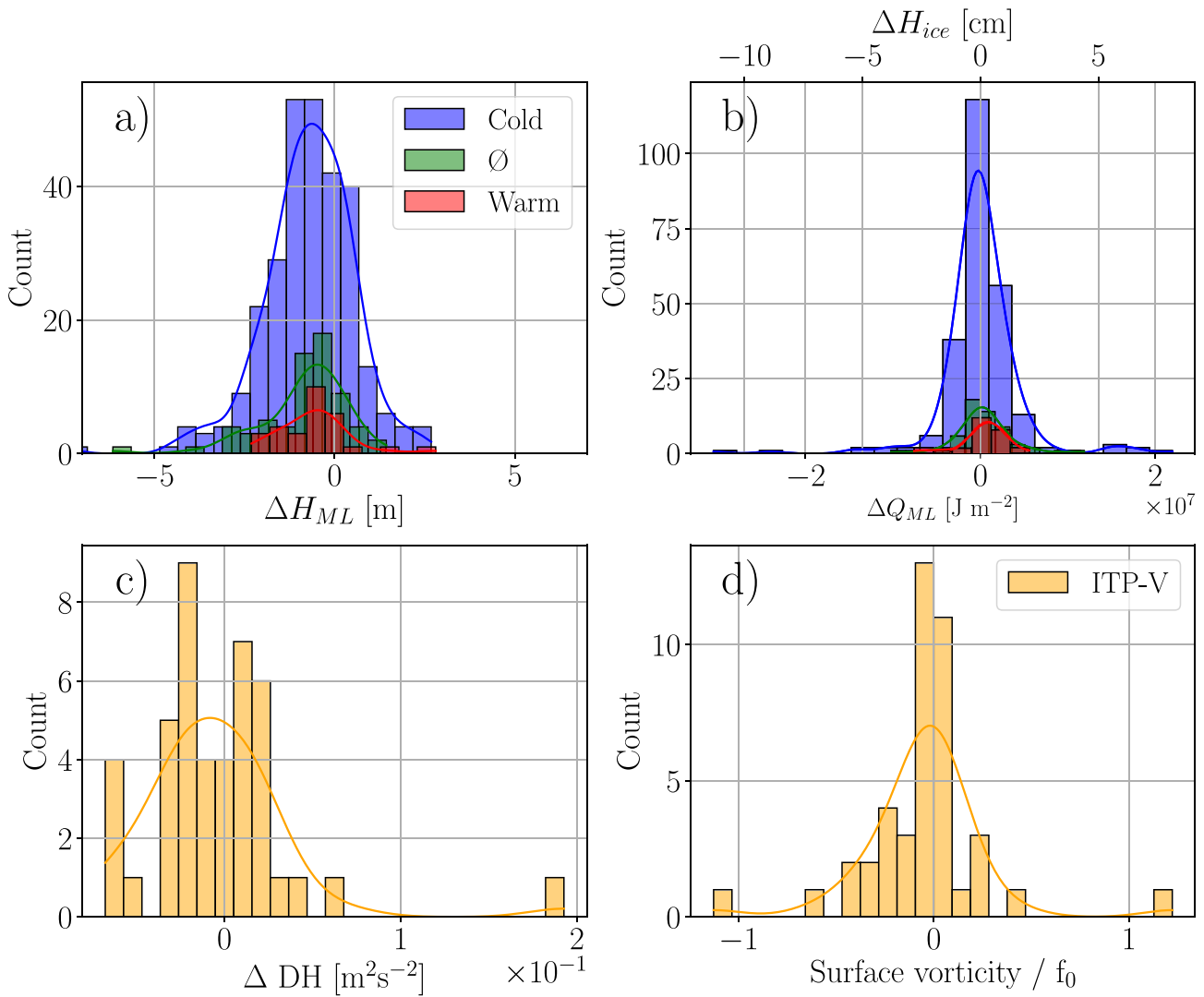


Figure 9. Probability density function of (a) the anomaly in mixed layer depth ΔH_{ML} , (b) the mixed layer heat content anomaly ΔQ_{ML} , and the sea ice thickness anomaly ΔH_{ice} , associated to the passage of a cold core eddy (blue), warm core eddy (red) or an eddy without any temperature anomaly (green), captured by ITP-V. Probability density function of (c) the surface Dynamic Height anomaly ΔDH and (d) the surface vorticity anomaly (normalized by f_0) inferred from ΔDH , for eddies captured by ITP-V.

For each eddy, we compute the gradient in DH at the surface between the eddy center and the eddy edge ($\Delta DH = DH_{center} - \frac{1}{2}\Sigma DH_{edge}$), and we compute the surface geostrophic velocity V_g associated to this gradient as:

$$V_g = \frac{\Delta DH}{f_0 R_{eddy}} \quad (5)$$

The associated surface vorticity anomaly is further estimated as $\epsilon = \frac{2V_g}{R_{eddy}}$. Given the need for an estimate of R_{eddy} and measurements in the surface layer, the calculation is only done for the eddies detected by the ITP-V.

Figures 9c and 9d shows the probability distribution of ΔDH , and the vorticity anomaly resulting from it. The distribution of ΔDH ranges from $-6 \times 10^{-2} m^2 s^{-2}$ to $5 \times 10^{-2} m^2 s^{-2}$, with an mean at $-0.4 \times 10^{-2} m^2 s^{-2}$. At first sight, it is surprising that the distribution of ΔDH is skewed to the left and negative values, despite the fact that most of the detected eddies are anticyclonic. In the case of anticyclonic meddies propagating at depth west of Gibraltar for instance, it was found that a positive sea level anomaly could be observed along their track (Bashmachnikov & Carton, 2012). Here, this is not the case and we find that many subsurface anticyclones are

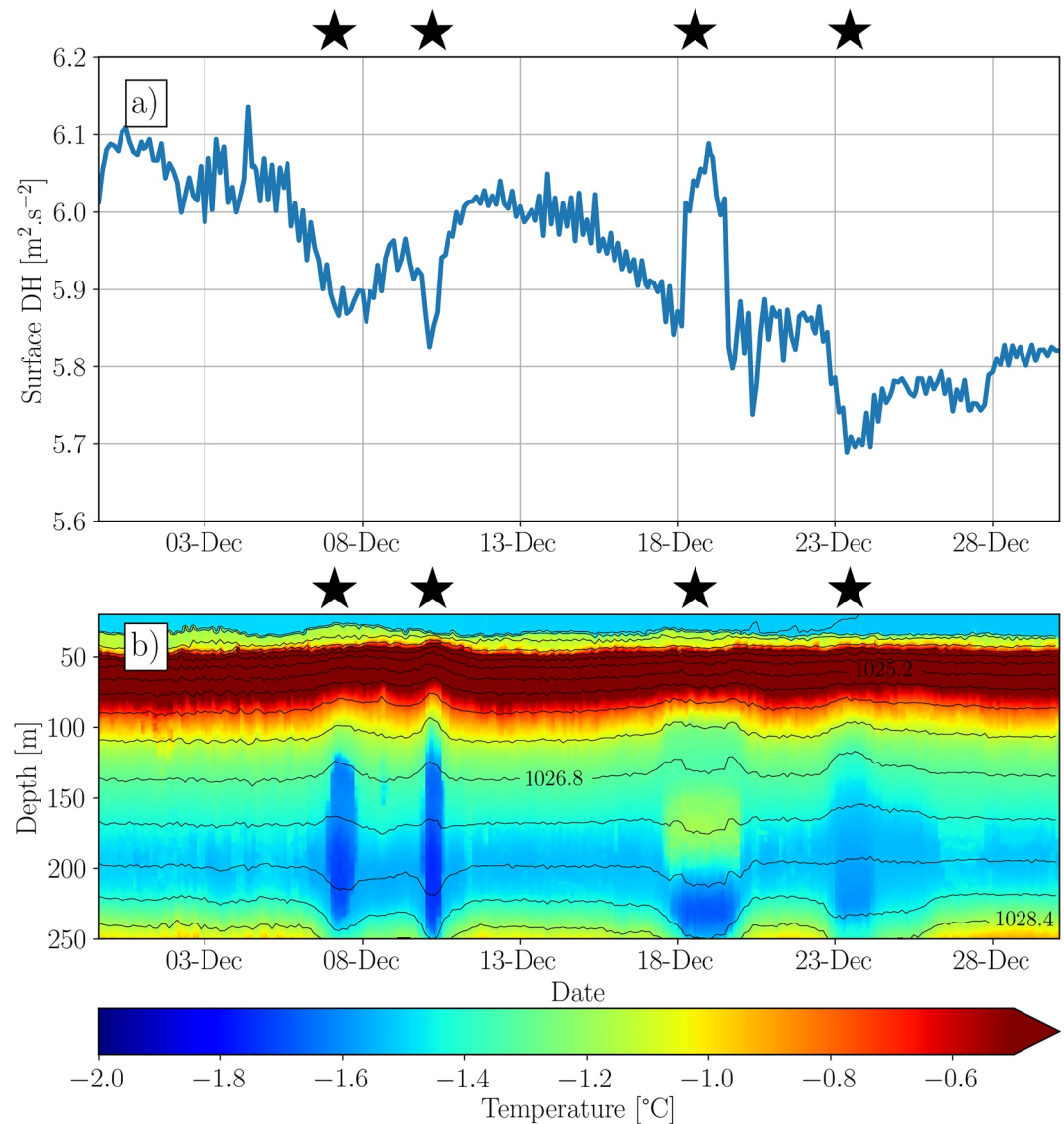


Figure 10. (a) Dynamic Height estimated at the surface and (b) temperature profiles for ITP-V 70 drifting in the Canadian Basin in winter 2013. The black lines on (b) correspond to isopycnal. The black stars indicate the position of the eddies.

associated with a negative anomaly in DH . In order to illustrate this behavior, we examine the case of one ITP-V (ITP-V 70) drifting in the Beaufort Gyre in 2013 (Figure 10). Between December 7 and December 24, the ITP crosses 4 anticyclones centered in the halocline, clearly identified by their cold temperature anomalies and the associated isopycnal displacement (Figure 10b). In the case of 3 out of these 4 eddies, the associated signature is a decrease in DH at the center of the eddy (Figure 10a). The eddy detected on December 18 appears to be a dipole, and is in contrast associated with a positive ΔDH of $2 \times 10^{-1} \text{m}^2 \text{s}^{-2}$. The sign of the surface signature, reverse to what we would have anticipated, is puzzling and we do not have a clear dynamical explanation for it. In order to check that it is not due to our choice of level of no motion, we have performed a few tests by estimating DH for a handful of eddies detected in ITP, and considering alternately 250 and 700 m as a reference level (not shown). Although the mean value of DH is indeed affected by the calculation method, with differences reaching around 15%, ΔDH remains of the same sign for the two reference levels for all cases. Further, we note that previous studies have highlighted similar counter-intuitive behaviors, when looking at the anomaly in sea surface temperature associated with the passage of eddies. While it is widely accepted that anticyclones (respectively cyclones) are associated with a cold (warm) core anomaly, an inverse signature in sea surface temperature has been found for some eddies in the Mediterranean Sea or the Tasman Sea (e.g., Everett et al., 2012; Hamad et al., 2006). Further

investigations would be required to fully understand the dynamical processes that determine the sign and intensity of the surface signature of the Arctic subsurface eddies, that likely involve some compensation of density anomalies within the water column. Overall, the large spread in the distribution of ΔDH further translates into a large range of values for the anomaly in surface normalized vorticity $\frac{\epsilon}{f_0}$, with values ranging from -1 to 1 and a maximum at -0.05 . These amplitudes are similar to the surface signature of meddies detected in the open ocean by Bashmachnikov and Carton (2012). This signal is an order of magnitude larger than the vorticity associated with a surface eddy in the MIZ of the Canadian Basin, that was found to induce a vorticity signature in sea ice (Cassianides et al., 2021). It thus suggests that the dynamical impact on sea ice of the subsurface eddies detected can be locally significant, and could possibly be detectable in satellite images from which the sea ice drift and vorticity can be retrieved.

6. Discussion and Conclusion

The dynamics of the Arctic Ocean at mesoscale and submesoscale remains poorly understood, despite their potential role for determining the sea ice conditions and their evolution. In this study, we present a detailed pan-Arctic characterization of the (sub)mesoscale variability over 16 years, making use of the large available datasets of in situ observations as extensively as possible. Based on a spectral analysis of the spatial potential density variance (which is equivalent to potential energy) sampled by ITP, we document a large variety of regimes that can be found under the sea ice pack. Indeed, both at the surface and at depth, one can find wavenumber spectra with slopes varying between -4 and -1 (Figure 3), regardless of the season, location or local sea ice conditions. Our results contrast with previous studies, based on a very limited sub-sample of our data set, that have suggested that the presence of sea ice would tend to damp the development of submesoscale instability, so that the dynamics would largely follow a quasi-geostrophic scaling even at the surface (Timmermans et al., 2012). Instead, our results showcase the complexity and heterogeneity of the dynamical regimes that appear to co-exist under the Arctic sea ice. In contrast, in the seasonal ice zone, the small scale dynamics seems to be easier to understand. On the one hand, at the surface, the time variations in KE are strongly anticorrelated with the sea ice thickness on a seasonal timescale, with KE that can reach as high as $10^{-2} \text{m}^2 \text{s}^{-2}$ in summer. On the other hand, at depth, the levels of energy remain unaffected by the variability in sea ice conditions. This is likely because the subsurface layer is largely isolated from the surface by the strong peak of stratification at the base of the surface layer (Meneghello et al., 2021).

Although we have tried our best to extract as much information as possible from the large observational data sets, it remains difficult to assemble a fully coherent picture of the small scale dynamics at the pan-Arctic scale. For instance, because ITPs are designed to sample the water column under thick sea ice, we are not able to perform the same diagnostics on potential energy in the regions that are seasonally ice-free. In the future, it would be interesting to examine data from surface and subsurface Lagrangian drifters sampling density continuously. Such analyses have been performed by Mensa et al. (2018) and Timmermans and Winsor (2013), but are thus far limited to very small datasets so that their representativeness might be questionable.

Nevertheless, the description of the pan-Arctic distribution of turbulence provided here suggests that, in the sea ice pack, the variability in sea ice conditions is not the primary driver for the variations in kinetic and potential energy. What about the other way around? Previous studies have exemplified that surface meso- and submeso-scale eddies can imprint a signature on sea ice, through both dynamical and thermodynamical processes (e.g., Gupta & Thompson, 2022; Manucharyan & Thompson, 2017). Yet, by performing a census of all eddies found in the Arctic over the period 2004–2019, we find that most eddies are found at depth, within the halocline layer. This raises the question of the potential impact of these subsurface eddies on sea ice, that we quantify based on simple qualitative diagnostics applied to each eddy individually. Figure 11 summarizes the different processes at play, in the case of an anticyclone (which represents 97% of our census). We find that the passage of a subsurface eddy is not associated with any significant change of the mixed layer depth nor its heat content, and thus does not induce any significant sea ice melt. This contrasts with the case of warm surface eddies that were observed to contribute locally to enhanced sea ice melt in the Chukchi Sea (Watanabe et al., 2014). We also estimate that most of the detected subsurface anticyclones modify the vertical stratification, and thus induce a significant anomaly in dynamical height at the surface (equivalent to a few centimeters in SSH). So far, available products of SSH for the Arctic (based on satellite altimetry retrieved in sea ice leads; e.g., Armitage et al., 2016) have a too coarse resolution both in time and space to allow for a direct detection of these anomalies as is routinely done in the

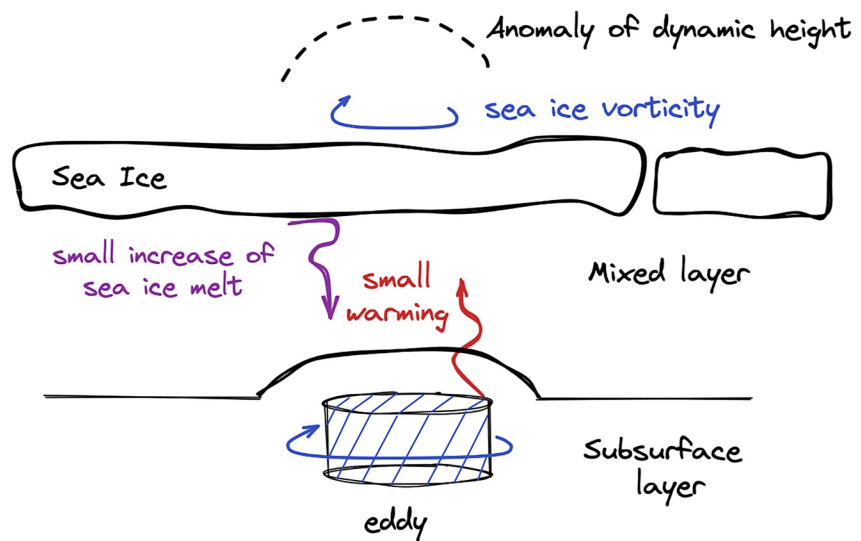


Figure 11. Schematic of the different processes involved in the interaction between a subsurface eddy (here an anticyclone) and sea ice.

open ocean (e.g., Faghmous et al., 2015). Instead, a detection of these subsurface eddies could potentially be done via the detection of sea ice vorticity retrieved for instance from SAR images (e.g., Cassianides et al., 2021), as the anomaly in vorticity at the ocean surface associated with the dynamical height anomaly appears to be strong enough to potentially induce an anomaly in sea ice vorticity. Further work will be required to determine the exact nature of such a signature in sea ice, that would likely depend on both the eddy characteristics (e.g., size, depth...) and the local sea ice conditions (thickness, presence of leads...). More generally, the importance of these local signatures for the evolution of the sea ice conditions at the pan-Arctic scale remains to be determined.

Data Availability Statement

The BGOS mooring data were collected and made available by the Beaufort Gyre Exploration Program based at the Woods Hole Oceanographic Institution in collaboration with researchers from Fisheries and Oceans Canada at the Institute of Ocean Sciences. ITP data were collected and made available by the ITP Program (Krishfield & Proshutinsky, 2006; Toole et al., 2011) based at the Woods Hole Oceanographic Institution. The datasets are publicly available in post-processed form at <https://www.whoi.edu/beaufortgyre> and <http://www.whoi.edu/itp>. Data from the Thermosalinograph (TSG) are available at <https://doi.pangaea.de/10.1594/PANGAEA.873145>. The sea ice concentration from OSISAF, product OSI-401-b (Tonboe et al., 2017), is available at <https://osi-saf.eumetsat.int/products/osi-401-b>.

Acknowledgments

This work was supported by the French ANR through the project ImMEDIAT (Grant ANR-18-CE01-0010), and a PhD studentship from Ifremer. G. M. was supported by NASA Grant 80NSSC21K0557. C.D.M. was supported by NASA Grant 80NSSC20K1140. We thank Carolina Dufour for a careful edit of the paper, and two anonymous reviewers for their constructive comments on the paper.

References

- Arbic, B. K., Scott, R. B., Flierl, G. R., Morten, A. J., Richman, J. G., & Shriver, J. F. (2012). Nonlinear cascades of surface oceanic geostrophic kinetic energy in the frequency domain. *Journal of Physical Oceanography*, 42(9), 1577–1600. <https://doi.org/10.1175/jpo-d-11-0151.1>
- Armitage, T. W. K., Bacon, S., Ridout, A. L., Thomas, S. F., Aksenov, Y., & Wingham, D. J. (2016). Arctic sea surface height variability and change from satellite radar altimetry and GRACE, 2003–2014. *Journal of Geophysical Research: Oceans*, 121(6), 4303–4322. <https://doi.org/10.1002/2015JC011579>
- Bashmachnikov, I., & Carton, X. (2012). Surface signature of Mediterranean water eddies in the Northeastern Atlantic: Effect of the upper ocean stratification. *Ocean Science*, 8(6), 931–943. <https://doi.org/10.5194/os-8-931-2012>
- Biddle, L. C., & Swart, S. (2020). The observed seasonal cycle of submesoscale processes in the Antarctic marginal ice zone. *Journal of Geophysical Research: Oceans*, 125(6), e2019JC015587. <https://doi.org/10.1029/2019JC015587>
- Blumen, W. (1978). Uniform potential vorticity flow: Part I. Theory of wave interactions and two-dimensional turbulence. *Journal of the Atmospheric Sciences*, 35(5), 774–783. [https://doi.org/10.1175/1520-0469\(1978\)035<0774:UPVFP1>2.0.CO;2](https://doi.org/10.1175/1520-0469(1978)035<0774:UPVFP1>2.0.CO;2)
- Boetius, A., & Rohardt, G. (2017). Continuous thermosalinograph oceanography along POLARSTERN cruise track PS101 (ARK-XXX/3). [Dataset]. PANGAEA. <https://doi.org/10.1594/PANGAEA.873145>
- Bramnigan, L., Johnson, H., Lique, C., Nycander, J., & Nilsson, J. (2017). Generation of subsurface anticyclones at Arctic surface fronts due to a surface stress. *Journal of Physical Oceanography*, 47(11), 2653–2671. <https://doi.org/10.1175/JPO-D-17-0022.1>
- Callies, J., & Ferrari, R. (2013). Interpreting energy and tracer spectra of upper-ocean turbulence in the submesoscale range (1–200 km). *Journal of Physical Oceanography*, 43(11), 2456–2474. <https://doi.org/10.1175/JPO-D-13-063.1>

- Callies, J., Ferrari, R., Klymak, J. M., & Gula, J. (2015). Seasonality in submesoscale turbulence. *Nature Communications*, 6(1), 1–8. <https://doi.org/10.1038/ncomms7862>
- Callies, J., Flierl, G., Ferrari, R., & Fox-Kemper, B. (2016). The role of mixed-layer instabilities in submesoscale turbulence. *Journal of Fluid Mechanics*, 788, 5–41. <https://doi.org/10.1017/jfm.2015.700>
- Carton, X., Sokolovskiy, M., Ménesguen, C., Aguiar, A., & Meunier, T. (2014). Vortex stability in a multi-layer quasi-geostrophic model: Application to Mediterranean water eddies. *Fluid Dynamics Research*, 46(6), 061401. <https://doi.org/10.1088/0169-5983/46/6/061401>
- Cassianides, A., Lique, C., & Korosov, A. (2021). Ocean eddy signature on SAR-derived sea ice drift and vorticity. *Geophysical Research Letters*, 48(6), e2020GL092066. <https://doi.org/10.1029/2020GL092066>
- Charney, J. G. (1971). Geostrophic turbulence. *Journal of the Atmospheric Sciences*, 28(6), 1087–1095. [https://doi.org/10.1175/1520-0469\(1971\)028<1087:GT>2.0.CO;2](https://doi.org/10.1175/1520-0469(1971)028<1087:GT>2.0.CO;2)
- Chelton, D. B., Schlax, M. G., & Samelson, R. M. (2011). Global observations of nonlinear mesoscale eddies. *Progress in Oceanography*, 91(2), 167–216. <https://doi.org/10.1016/j.pocean.2011.01.002>
- Cole, S. T., Thwaites, F. T., Krishfield, R. A., & Toole, J. M. (2015). Processing of velocity observations from ice-tethered profilers. In *Oceans 2015 - MTS/IEEE Washington* (pp. 1–10). IEEE. <https://doi.org/10.23919/OCEANS.2015.7401887>
- D'Asaro, E. A. (1988). Generation of submesoscale vortices: A new mechanism. *Journal of Geophysical Research*, 93(C6), 6685. <https://doi.org/10.1029/JC093IC06P06685>
- Davis, P. E. D., Lique, C., Johnson, H. L., & Guthrie, J. D. (2016). Competing effects of elevated vertical mixing and increased freshwater input on the stratification and sea ice cover in a changing Arctic Ocean. *Journal of Physical Oceanography*, 46(5), 1531–1553. <https://doi.org/10.1175/JPO-D-15-0174.1>
- Doddridge, E. W., Meneghello, G., Marshall, J., Scott, J., & Lique, C. (2019). A three-way balance in the Beaufort Gyre: The Ice–Ocean Governor, wind stress, and eddy diffusivity. *Journal of Geophysical Research: Oceans*, 124(5), 3107–3124. <https://doi.org/10.1029/2018JC014897>
- Everett, J. D., Baird, M. E., Oke, P. R., & Suthers, I. M. (2012). An avenue of eddies: Quantifying the biophysical properties of mesoscale eddies in the Tasman Sea. *Geophysical Research Letters*, 39(16). <https://doi.org/10.1029/2012GL053091>
- Faghmous, J. H., Frenger, I., Yao, Y., Warmka, R., Lindell, A., & Kumar, V. (2015). A daily global mesoscale ocean eddy dataset from satellite altimetry. *Scientific Data*, 2(1), 150028. <https://doi.org/10.1038/sdata.2015.28>
- Ferrari, R., & Wunsch, C. (2010). The distribution of eddy kinetic and potential energies in the global ocean. *Tellus A*, 62(2), 92–108. <https://doi.org/10.1111/j.1600-0870.2009.00432.x>
- Giddy, I., Swart, S., du Plessis, M., Thompson, A. F., & Nicholson, S. (2021). Stirring of sea-ice meltwater enhances submesoscale fronts in the Southern Ocean. *Journal of Geophysical Research: Oceans*, 126(4). <https://doi.org/10.1029/2020JC016814>
- Giulivi, C. F., & Gordon, A. L. (2006). Isopycnal displacements within the Cape Basin thermocline as revealed by the hydrographic data archive. *Deep Sea Research Part I: Oceanographic Research Papers*, 53(8), 1285–1300. <https://doi.org/10.1016/j.dsr.2006.05.011>
- Gupta, M., Marshall, J., Song, H., Campin, J.-M., & Meneghello, G. (2020). Sea-ice melt driven by ice-ocean stresses on the mesoscale. *Journal of Geophysical Research: Oceans*, 125(11), e2020JC016404. <https://doi.org/10.1029/2020JC016404>
- Gupta, M., & Thompson, A. F. (2022). Regimes of sea-ice floe melt: Ice-ocean coupling at the submesoscales. *Journal of Geophysical Research: Oceans*, 127(9), e2022JC018894. <https://doi.org/10.1029/2022JC018894>
- Hamad, N., Millot, C., & Taupier-Letage, I. (2006). The surface circulation in the eastern basin of the Mediterranean Sea. *Scientia Marina*, 70(3), 457–503. <https://doi.org/10.3989/scimar.2006.70n3457>
- Horvat, C., Tziperman, E., & Campin, J.-M. (2016). Interaction of sea ice floe size, ocean eddies, and sea ice melting. *Geophysical Research Letters*, 43(15), 8083–8090. <https://doi.org/10.1002/2016GL069742>
- Johannessen, J., Johannessen, O., Svendsen, E., Shuchman, R., Manley, T., Campbell, W., et al. (1987). Mesoscale eddies in the Fram Strait marginal ice zone during the 1983 and 1984 marginal ice zone experiments. *Journal of Geophysical Research*, 92(C7), 6754–6772. <https://doi.org/10.1029/jc092ic07p06754>
- Johannessen, O. M., Johannessen, J. A., Svendsen, E., Shuchman, R. A., Campbell, W. J., & Josberger, E. (1987). Ice-edge eddies in the Fram Strait marginal ice zone. *Science*, 236(4800), 427–429. <https://doi.org/10.1126/science.236.4800.427>
- Klein, P., Hua, B. L., Lapeyre, G., Capet, X., Le Gentil, S., & Sasaki, H. (2008). Upper Ocean turbulence from high-resolution 3D simulations. *Journal of Physical Oceanography*, 38(8), 1748–1763. <https://doi.org/10.1175/2007JPO3773.1>
- Kozlov, I. E., Artamonova, A. V., Manucharyan, G. E., & Kubryakov, A. A. (2019). Eddies in the Western Arctic Ocean from spaceborne SAR observations over open ocean and marginal ice zones. *Journal of Geophysical Research: Oceans*, 124(9), 6601–6616. <https://doi.org/10.1029/2019JC015113>
- Kozlov, I. E., Plotnikov, E. V., & Manucharyan, G. E. (2020). Brief communication: Mesoscale and submesoscale dynamics in the marginal ice zone from sequential synthetic aperture radar observations. *The Cryosphere*, 14(9), 2941–2947. <https://doi.org/10.5194/tc-14-2941-2020>
- Krishfield, R., & Proshutinsky, A. (2006). *BGOS ULS data processing procedure (Technical report)*. Woods Hole Oceanographic Institution.
- Lique, C., Guthrie, J. D., Steele, M., Proshutinsky, A., Morison, J. H., & Krishfield, R. (2014). Diffusive vertical heat flux in the Canada Basin of the Arctic Ocean inferred from moored instruments. *Journal of Geophysical Research: Oceans*, 119(1), 496–508. <https://doi.org/10.1002/2013JC009346>
- Lique, C., & Steele, M. (2013). Seasonal to decadal variability of Arctic Ocean heat content: A model-based analysis and implications for autonomous observing systems. *Journal of Geophysical Research: Oceans*, 118(4), 1673–1695. <https://doi.org/10.1002/jgrc.20127>
- Manley, T. O., & Hunkins, K. (1985). Mesoscale eddies of the Arctic Ocean. *Journal of Geophysical Research*, 90(C3), 4911. <https://doi.org/10.1029/jc090ic03p04911>
- Manucharyan, G. E., Lopez-Acosta, R., & Wilhelmus, M. M. (2022). Spinning ice floes reveal intensification of mesoscale eddies in the Western Arctic Ocean. *Scientific Reports*, 12(1), 7070. <https://doi.org/10.1038/s41598-022-10712-z>
- Manucharyan, G. E., & Thompson, A. F. (2017). Submesoscale Sea Ice–Ocean interactions in marginal ice zones. *Journal of Geophysical Research: Oceans*, 122(12), 9455–9475. <https://doi.org/10.1002/2017JC012895>
- Marcinko, C. L., Martin, A. P., & Allen, J. T. (2015). Characterizing horizontal variability and energy spectra in the Arctic Ocean halocline. *Journal of Geophysical Research: Oceans*, 120(1), 436–450. <https://doi.org/10.1002/2014JC010381>
- McWilliams, J. C. (2016). *Submesoscale currents in the ocean* (Vol. 472). Royal Society of London. No. 2189. <https://doi.org/10.1098/rspa.2016.0117>
- Meier, W. N., & Stroeve, J. (2022). An updated assessment of the changing Arctic Sea Ice cover. *Oceanography*, 35(2). <https://doi.org/10.5670/OCEANOGRAPHY.2022.114>
- Meneghello, G., Marshall, J., Lique, C., Isachsen, P. E., Doddridge, E., Campin, J.-M., et al. (2021). Genesis and decay of mesoscale baroclinic eddies in the seasonally ice-covered interior Arctic Ocean. *Journal of Physical Oceanography*, 51(1), 115–129. <https://doi.org/10.1175/JPO-D-20-0054.1>

- Mensa, J. A., & Timmermans, M. L. (2017). Characterizing the seasonal cycle of upper-ocean flows under multi-year sea ice. *Ocean Modelling*, *113*, 115–130. <https://doi.org/10.1016/j.ocemod.2017.03.009>
- Mensa, J. A., Timmermans, M.-L., Kozlov, I. E., Williams, W. J., & Özgökmen, T. M. (2018). Surface drifter observations from the Arctic Ocean's Beaufort Sea: Evidence for submesoscale dynamics. *Journal of Geophysical Research: Oceans*, *123*(4), 2635–2645. <https://doi.org/10.1002/2017JC013728>
- Meredith, M., Sommerkorn, M., Cassotta, S., Derksen, C., Ekaykin, A., Hollowed, A., et al. (Eds.). IPCC special report on the ocean and cryosphere in a changing climate (pp. 203–320). Cambridge University Press. <https://doi.org/10.1017/9781009157964.005>
- Newton, J. L., Aagaard, K., & Coachman, L. K. (1974). Baroclinic eddies in the Arctic Ocean. *Deep-Sea Research and Oceanographic Abstracts*, *21*(9), 707–719. [https://doi.org/10.1016/0011-7471\(74\)90078-3](https://doi.org/10.1016/0011-7471(74)90078-3)
- Nurser, A. J. G., & Bacon, S. (2014). The Rossby radius in the Arctic Ocean. *Ocean Science*, *10*(6), 967–975. <https://doi.org/10.5194/os-10-967-2014>
- Ou, H. W., & Gordon, A. L. (1986). Spin-down of baroclinic eddies under sea ice. *Journal of Geophysical Research*, *91*(C6), 7623. <https://doi.org/10.1029/jc091ic06p07623>
- Peralta-Ferriz, C., & Woodgate, R. A. (2015). Seasonal and interannual variability of pan-Arctic surface mixed layer properties from 1979 to 2012 from hydrographic data, and the dominance of stratification for multiyear mixed layer depth shoaling. *Progress in Oceanography*, *134*, 19–53. <https://doi.org/10.1016/j.pocean.2014.12.005>
- Perovich, D. K., & Richter-Menge, J. A. (2015). Regional variability in sea ice melt in a changing Arctic. *Philosophical Transactions of the Royal Society A: Mathematical, Physical & Engineering Sciences*, *373*(2045), 20140165. <https://doi.org/10.1098/rsta.2014.0165>
- Pickart, R. S., & Stossmeister, G. (2008). Outflow of Pacific water from the Chukchi Sea to the Arctic Ocean. *Advances in Polar Science*, *10*, 135–148.
- Pnyushkov, A., Polyakov, I. V., Padman, L., & Nguyen, A. T. (2018). Structure and dynamics of mesoscale eddies over the Laptev Sea continental slope in the Arctic Ocean. *Ocean Science*, *14*(5), 1329–1347. <https://doi.org/10.5194/os-14-1329-2018>
- Proshutinsky, A., Krishfield, R., Timmermans, M.-L., Toole, J., Carmack, E., McLaughlin, F., et al. (2009). Beaufort Gyre freshwater reservoir: State and variability from observations. *Journal of Geophysical Research*, *114*, C00A10. <https://doi.org/10.1029/2008JC005104>
- Regan, H., Lique, C., & Armitage, T. W. K. (2019). The Beaufort Gyre extent, shape, and location between 2003 and 2014 from satellite observations. *Journal of Geophysical Research: Oceans*, *124*(2), 844–862. <https://doi.org/10.1029/2018JC014379>
- Regan, H., Lique, C., Talandier, C., & Meneghello, G. (2020). Response of total and eddy kinetic energy to the recent spinup of the Beaufort Gyre. *Journal of Physical Oceanography*, *50*(3), 575–594. <https://doi.org/10.1175/JPO-D-19-0234.1>
- Rheinlander, J. W., Davy, R., Ólason, E., Rampal, P., Spensberger, C., Williams, T. D., et al. (2022). Driving mechanisms of an extreme winter sea ice breakup event in the Beaufort Sea. *Geophysical Research Letters*, *49*(12), e2022GL099024. <https://doi.org/10.1029/2022GL099024>
- Shimada, K., Itoh, M., Nishino, S., McLaughlin, F., Carmack, E., & Proshutinsky, A. (2005). Halocline structure in the Canada Basin of the Arctic Ocean. *Geophysical Research Letters*, *32*(3), L03605. <https://doi.org/10.1029/2004gl021358>
- Shrestha, K., & Manucharyan, G. E. (2022). Parameterization of submesoscale mixed layer restratification under sea ice. *Journal of Physical Oceanography*, *52*(3), 419–435. <https://doi.org/10.1175/JPO-D-21-0024.1>
- Spall, M. A. (2013). On the circulation of Atlantic water in the Arctic Ocean. *Journal of Physical Oceanography*, *43*(11), 2352–2371. <https://doi.org/10.1175/JPO-D-13-079.1>
- Supply, A., Boutin, J., Vergely, J.-L., Kolodziejczyk, N., Reverdin, G., Reul, N., & Tarasenko, A. (2020). New insights into SMOS sea surface salinity retrievals in the Arctic Ocean. *Remote Sensing of Environment*, *249*, 112027. <https://doi.org/10.1016/j.rse.2020.112027>
- Thompson, A. F., Lazar, A., Buckingham, C., Garabato, A. C. N., Damerell, G. M., & Heywood, K. J. (2016). Open-ocean submesoscale motions: A full seasonal cycle of mixed layer instabilities from gliders. *Journal of Physical Oceanography*, *46*(4), 1285–1307. <https://doi.org/10.1175/JPO-D-15-0170.1>
- Thomson, R. E., & Emery, W. J. (2014). Time series analysis methods. *Data Analysis Methods in Physical Oceanography*, 425–591. <https://doi.org/10.1016/B978-0-12-387782-6.00005-3>
- Timmermans, M. L., Cole, S., & Toole, J. (2012). Horizontal density structure and restratification of the Arctic Ocean surface layer. *Journal of Physical Oceanography*, *42*(4), 659–668. <https://doi.org/10.1175/JPO-D-11-0125.1>
- Timmermans, M. L., & Winsor, P. (2013). Scales of horizontal density structure in the Chukchi Sea surface layer. *Continental Shelf Research*, *52*, 39–45. <https://doi.org/10.1016/j.csr.2012.10.015>
- Tonboe, R., Lavelle, J., Pfeiffer, R.-H., & Howe, E. (2017). *Ocean & Sea Ice SAF product user manual for OSI SAF global sea ice concentration (Technical Report)*. Danish Meteorological Institute.
- Toole, J., Krishfield, R., Timmermans, M.-L., & Proshutinsky, A. (2011). The ice-tethered profiler: Argo of the Arctic. *Oceanography*, *24*(3), 126–135. <https://doi.org/10.5670/oceanog.2011.64>
- von Appen, W. J., Baumann, T. M., Janout, M., Koldunov, N., Lenn, Y. D., Pickart, R. S., et al. (2022). Eddies and the distribution of eddy kinetic energy in the Arctic Ocean. *Oceanography*, *35*(2). <https://doi.org/10.5670/OCEANOGRAPHY.2022.122>
- von Appen, W.-J., Wekerle, C., Hehemann, L., Schourup-Kristensen, V., Konrad, C., & Iversen, M. H. (2018). Observations of a submesoscale cyclonic filament in the marginal ice zone. *Geophysical Research Letters*. <https://doi.org/10.1029/2018GL077897>
- Wang, Q., Koldunov, N. V., Danilov, S., Sidorenko, D., Wekerle, C., Scholz, P., et al. (2020). Eddy kinetic energy in the Arctic Ocean from a global simulation with a 1-km Arctic. *Geophysical Research Letters*, *47*(14), e2020GL088550. <https://doi.org/10.1029/2020GL088550>
- Watanabe, E., Onodera, J., Harada, N., Honda, M. C., Kimoto, K., Kikuchi, T., et al. (2014). Enhanced role of eddies in the arctic marine biological pump. *Nature Communications*, *5*(1), 1–12. <https://doi.org/10.1038/ncomms4950>
- Woodgate, R. A., Aagaard, U., Muench, R. D., Gunn, J., Oran Bjj Ork, G. G., Rudels, B., et al. (2000). The Arctic Ocean boundary current along the Eurasian slope and the adjacent Lomonosov Ridge: Water mass properties, transports and transformations from moored instruments. (Technical report no. 1).
- Zhang, Y., Maslowski, W., & Semtner, A. J. (1999). Impact of mesoscale ocean currents on sea ice in high-resolution Arctic ice and ocean simulations. *Journal of Geophysical Research*, *104*(C8), 18409–18429. <https://doi.org/10.1029/1999jc900158>
- Zhao, M., Timmermans, M., Krishfield, R., & Manucharyan, G. (2018). Partitioning of kinetic energy in the Arctic Ocean's Beaufort Gyre. *Journal of Geophysical Research: Oceans*, *123*(7), 4806–4819. <https://doi.org/10.1029/2018JC014037>
- Zhao, M., Timmermans, M.-L., Cole, S., Krishfield, R., Proshutinsky, A., & Toole, J. (2014). Characterizing the eddy field in the Arctic Ocean halocline. *Journal of Geophysical Research: Oceans*, *119*(12), 8800–8817. <https://doi.org/10.1002/2014JC010488>
- Zhao, M., Timmermans, M.-L., Cole, S., Krishfield, R., & Toole, J. (2016). Evolution of the eddy field in the Arctic Ocean's Canada Basin, 2005–2015. *Geophysical Research Letters*, *43*(15), 8106–8114. <https://doi.org/10.1002/2016GL069671>